



Virginia Commonwealth University  
VCU Scholars Compass

---

Theses and Dissertations

Graduate School

---

2024

## Measuring the Properties of Rod-Shaped Bacteria by Single-Entity Electrochemistry

Ashley Tubbs  
*Virginia Commonwealth University*

Follow this and additional works at: <https://scholarscompass.vcu.edu/etd>

 Part of the [Analytical Chemistry Commons](#)

© The Author

---

Downloaded from

<https://scholarscompass.vcu.edu/etd/7706>

This Dissertation is brought to you for free and open access by the Graduate School at VCU Scholars Compass. It has been accepted for inclusion in Theses and Dissertations by an authorized administrator of VCU Scholars Compass. For more information, please contact [libcompass@vcu.edu](mailto:libcompass@vcu.edu).

VIRGINIA COMMONWEALTH UNIVERSITY

**Measuring the Properties of Rod-Shaped Bacteria by Single-Entity Electrochemistry**

A dissertation submitted in partial fulfillment of the requirements for the degree of

DOCTOR OF PHILOSOPHY

in Chemistry

at Virginia Commonwealth University

by

**Ashley Tubbs**

Dissertation Committee

Associate Professor Julio C. Alvarez, Chair  
John B. Fenn Professor in Chemistry Maryanne Collinson  
Assistant Professor Ka Un Lao  
Associate Professor Dexian Ye

2024

© Ashley Tubbs

# Table of Contents

<b>Acknowledgments</b> .....	<b>v</b>
<b>Abstract</b> .....	<b>vii</b>
<b>Chapter 1. Fundamentals of Electrochemistry and Other Important Principles</b> .....	<b>1</b>
1.1. Redox Processes in Electrochemical Systems .....	1
1.2. The Electrical Double Layer .....	6
1.3. Mass Transport Mechanisms .....	10
1.4. Cyclic Voltammetry .....	15
1.4.1. Cyclic Voltammetry at Macroelectrodes.....	15
1.4.2. Cyclic Voltammetry at Ultramicroelectrodes .....	17
1.5. Chronoamperometry .....	20
<b>Chapter 2. Fundamentals of Single-Entity Electrochemistry and Other Important Principles</b> .....	<b>22</b>
2.1. Insulating Particles .....	23
2.2. Single-Entity Electrochemistry.....	24
2.2.1. Types of Signals.....	24
2.2.2. Recent Advances in Blocking Electrochemistry .....	27
2.3. Complementary Methods .....	33
2.3.1. Dynamic Light Scattering .....	33
2.3.2. Zeta Potential.....	34
2.3.3. UV-vis Spectroscopy .....	36
<b>Chapter 3. Electrochemical Detection of Rod-shaped Bacteria by Blocking Electrochemistry</b> .....	<b>37</b>
3.1. Introduction .....	37
3.2. Experimental .....	38
3.2.1. Chemical Reagents.....	38
3.2.2. Instrumentation .....	38
3.2.3. Ultramicroelectrode Fabrication.....	39
3.2.4. Cell Culturing and Bacteria Preparation .....	40
3.3. Results and Discussion .....	40
3.3.1. Experimental Conditions for Blocking Signals by Bacterial Cells .....	40
3.3.2. Diffusion Coefficients of Bacterial Cells .....	45

3.3.3. Effect of $\gamma$ on Collisional Frequency .....	47
3.4. Conclusions .....	51
<b>Chapter 4. Bacterial Identification in Mixed Samples .....</b>	<b>53</b>
4.1. Introduction .....	53
4.2. Experimental .....	54
4.2.1. Chemical Reagents .....	54
4.2.2. Instrumentation .....	54
4.2.3. Cell Culturing and Bacteria Preparation .....	55
4.2.4. Data Collection and Analysis .....	55
4.3. Results and Discussion .....	56
4.3.1. Convolution of Bacterial <i>i-t</i> Curve by Application of First Derivative Savitzky-Golay Filter	56
4.3.2. Discrimination of <i>A. erythreum</i> and <i>B. subtilis</i> in Mixed Samples.....	63
4.4. Conclusions .....	66
<b>Chapter 5. Electrochemical Determination of Cell Viability .....</b>	<b>67</b>
5.1. Introduction .....	67
5.2. Experimental .....	69
5.2.1. Chemical Reagents .....	69
5.2.2. Instrumentation .....	69
5.2.3. Cell Culturing and Bacteria Preparation .....	70
5.2.4. Data Collection and Analysis .....	70
5.3. Results and Discussion .....	71
5.3.1. Effect of Valinomycin on Zeta Potential and Observed Chronoamperometric Signal of <i>B. subtilis</i> .....	71
5.4. Conclusions .....	75
<b>Conclusions and Future Work .....</b>	<b>76</b>

## Acknowledgments

I would like to first thank my advisor, Dr. Julio Alvarez, for always encouraging me to work independently. This work would not have been possible without your guidance and support, and I will carry much of what you have taught me going forward.

I would like to thank my committee for their invaluable and constructive feedback throughout my time as a graduate student at Virginia Commonwealth University.

My fellow Alvarez group members for their support and encouragement in the work completed herein.

The undergraduate research students I have had the pleasure to mentor these past four years. For bringing your enthusiasm and inquisitive minds into the laboratory. I am honored to call many of you my close friends.

Katie Hergenrother, for the boxes of goodies and decorations to remind me to get out of my head and celebrate the holidays. I truly could not have done this without your support.

Dr. Megan Chambers, for the late-night phone calls and Zoom meetings to vent about research woes. For being an incredible scientist and best friend.

Dr. Lisa Graves, for the weekly coffee runs to catch up on our lives and remind each other that there is life outside the lab.

Dr. Julian Bobb, for introducing me to the wonderful volunteer opportunities in the American Chemical Society and Younger Chemists Committee.

My parents, John and Brenda, for their unconditional love and support as I navigated graduate school. For sending me pictures of my cat, Devi, and keeping me updated on my brothers.

My found family at Bridges, for accepting me for who I am and encouraging me to come out of my shell.

The College of Humanities and Sciences and the Chemistry Department, for their generous financial support, particularly this semester to complete this dissertation.

## Abstract

Antibiotic-resistant bacteria pose a significant and escalating threat to hospitals around the world, necessitating the development of rapid and sensitive detection methods. Single-entity electrochemistry, an electrochemical technique first reported in 2004, has emerged as a promising approach for detecting and identifying such bacteria and monitoring the efficacy of antibiotics in real-time. The technique's power lies in the working electrode, typically a disk ultramicroelectrode with a radius smaller than 25  $\mu\text{m}$ , being on the same size scale as the particle it is being used to detect. With this setup, the interactions of single particles with the electrode surface can be electrochemically detected and quantified. In the years following the initial report, single-entity electrochemistry was used to quantify the interactions of metal nanoparticles, polymer beads, and emulsion droplets. In 2015, single entity electrochemistry was used to detect bacteria for the first time. However, current work with bacterial sensing by single-entity electrochemistry is generally limited to detecting bacterial cells and correlating their interactions with the electrode surface to the signals observed in chronoamperograms.

To fully understand single-entity electrochemistry, the underlying electrochemical principles must be well understood. To that end, **Chapter 1** focuses on the fundamentals of general electrochemistry, and electrochemical techniques that are relevant to this work. To provide a well-rounded background, **Chapter 2** provides an in-depth look at recent work in the field of single-entity electrochemistry, including the types of signals that can be generated and drawing on work done with many types of analytes to supplement this work. Further, a summary of complementary techniques used in this work, including dynamic light scattering (DLS) and zeta potential, are discussed. Finally, **Chapters 3-5** are dedicated to the work performed with regards to this dissertation, focusing first on the detection and identification of bacteria by single-entity electrochemistry, then the technique's use as a monitor for antibiotic efficacy.

In **Chapter 3**, we employ the translational diffusion equation for circular cylinders to predict the collision frequency of rod-shaped bacteria under diffusion-controlled and migration-controlled conditions, informing our experimental setup. Our work demonstrates that lab-fabricated Pt ultramicroelectrodes can sensitively detect the adsorption of bacteria at femtomolar concentrations under migration-controlled conditions. However, the experimental frequency is significantly lower than predicted by the migration-controlled frequency calculation. To explore the underlying cause, the ratio of supporting electrolyte and redox species (two parameters affecting the movement of a particle to the electrode surface) is manipulated to induce both migration and diffusion. We find that the adsorption frequency changes very little with the increasing ratio, up to a 10:1 ratio of supporting electrolyte concentration to redox species concentration.

In **Chapter 4**, we present a method implemented in MatLab to automate the analysis of the step-like signals observed in chronoamperograms. By applying a quadratic first-derivative Savitzky-Golay filter to the signals, we transform the step-like signals to spike-like signals, facilitating less-biased quantification of the magnitude of current change caused by bacterial adsorption. Integration of the area under each peak allows us to quickly determine the magnitude of current change and the time corresponding to the bacteria adsorbing to the electrode surface. The efficacy of the filter and integration are compared to results obtained with manual analysis of the *i-t* curves, which generally show good agreement. Larger discrepancies are observed in the temporal domain than the amperometric domain, which is ascribed to the deviation from a flat baseline being more obvious than from a sloping baseline. With this powerful tool, we demonstrate the potential to distinguish two discrete bacteria species, *Aeromicrobium erythreum* and *Bacillus subtilis*, within mixed samples by generating bi-dimensional population density plots of the step magnitudes.

Finally, in **Chapter 5**, we test the capability of our system to monitor the response of *B. subtilis* following exposure to the dodecapeptide antibiotic valinomycin, which has been shown to

inhibit the proton-motive force across the cellular membrane. Zeta potential monitoring shows a slight decrease in the magnitude of the bacterial zeta potential post-valinomycin exposure, which remains constant over two hours. Interestingly, the observed signal changes post-exposure, from step-like signals to hump-like signals, then back to step-like signals. The hump-like signals are attributed to interactions between inhibited bacteria and the electrode surface. These findings underscore the potential of single-entity electrochemistry for rapid bacterial detection and identification, and antibiotic efficacy assessment, offering valuable insights into combatting antibiotic resistance in clinical settings.

# Chapter 1

## Fundamentals of Electrochemistry and Other Important Principles

This chapter provides an overview of a select few key concepts in general electrochemistry, including redox processes in electrochemical systems, the double layer, zeta potential, and mass transport. Additionally, some basic electrochemical techniques, such as cyclic voltammetry and chronoamperometry are presented to facilitate understanding of the work described in later chapters.

### 1.1. Redox Processes in Electrochemical Systems

In general, oxidation-reduction reactions are understood as processes involving the transfer of electrons between an oxidizing species and a reducing species. This transfer of electrons arises from the difference in their propensity to gain electrons (reduction) or lose electrons (oxidation), forming new, more stable species as a result.<sup>1</sup> The propensity of the individual reactants to undergo oxidation or reduction is described by the specific chemical potential of each species. In an electrochemical system, one of these chemical species is typically replaced by an electrode, facilitating electron transfer between the electrode and an electroactive redox species. Here, the propensity of the system to transfer electrons between the redox species and the electrode is described by the electrode potential.

Reversible electron transfer in an aqueous electrochemical solution can be generally described by Equation (1)



where  $O_{(aq)}^z$  represents the oxidized species and  $R_{(aq)}^{z-n}$  represents the reduced species in an aqueous solution, with  $z$  denoting the oxidation number, and  $n$  representing the number of

transferred electrons,  $e^-$ , within the electrode phase. This electrode, where reactions of interest occur, is generally termed the working electrode. For a working electrode with a negative charge, equilibrium is shifted to the right from the electron-rich side following Le Chatelier's Principle. Conversely, for a working electrode with a positive charge, equilibrium is shifted to the left from the electron-deficient side. The resultant charge separation between the working electrode and the solution generates an interfacial potential difference. However, it is impossible to measure the potential of a single electrode. By necessity, a second electrode of a near-constant composition is introduced to the aqueous solution.<sup>1</sup> The potential of this electrode is constant and stable, so that the potential of the working electrode can be referenced to it, thus making the electrochemical measurements measurable and meaningful. In aqueous solutions, many types of reference electrodes can be used. The standard hydrogen electrode (SHE) is the internationally accepted reference electrode, and as such is arbitrarily assigned a value of zero ( $E^0 = 0.00\text{ V}$ ). Two commonly used reference electrodes are the saturated calomel electrode (SCE) and the silver-silver chloride (Ag/AgCl) electrode, which have potentials of 0.242 V vs. SHE and 0.197 V vs SHE, respectively.

For the electrochemical system described above, one can measure the difference in electric potential between the working and reference electrodes using a high impedance voltmeter. This *cell potential* can be controlled by an external power supply, such as a battery. To drive a non-spontaneous reaction in the electrochemical cell, a negative charge is applied to the working electrode, the energy of the electrons in the metal is raised, until a critical potential is reached that allow the transfer of electrons from the electrode to  $O_{(aq)}^z$ , creating a flow of electrons termed a current.<sup>2</sup> The additional potential,  $E$ , beyond the equilibrium potential,  $E_{eq}$ , required to drive this non-spontaneous reaction is termed the *overpotential*,  $\eta$ , according to Equation (2),

$$\eta = E - E_{eq} \quad (2)$$

To practically measure the *Faradaic* current in an electrochemical system, a third electrode, the counter electrode, is connected to the working electrode. A simplified schematic of the three-electrode setup is shown in **Figure 1**. Ideally, the counter electrode has a large surface area, good conductance, and is made of a material that is chemically inert, to avoid unwanted side reactions that may interfere with the signal measured at the working electrode. These properties of the counter electrode ensure that its open circuit potential will remain constant and ohmic drop will be minimized.<sup>3</sup> Ohmic drop, or the potential difference, is proportional to the resistance of the solution during current flow through the electrochemical cell, following Ohm's Law:

$$E = -iR_{sol} \quad (3)$$

where  $i$  is the current flowing through the electrochemical cell and  $R_{sol}$  is the resistance of the solution. The amount of current passed through the cell can be related stoichiometrically to Equation (1) by Faraday's constant:

$$Q = it = nFN \quad (4)$$

where  $Q$  is the charge in coulombs (C),  $t$  is the time over which the charge is measured in seconds,  $n$  is the number of electrons per molecules of product,  $F$  is Faraday's constant, and  $N$  is the number of moles of product.<sup>4</sup>

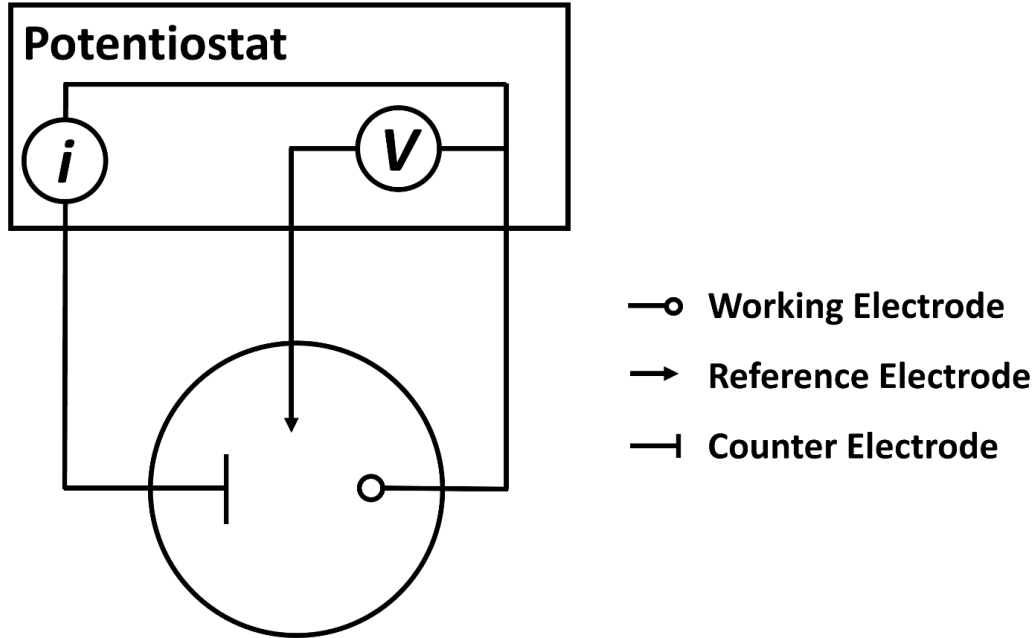


**Figure 1:** Simplified schematic of a three-electrode setup.

If we consider a simplified version of Equation (1), where  $n = 1$ ,



where  $k_f$  and  $k_b$  are the forward and backward rate constants, respectively. The net current can be given as the difference between the anodic ( $i_a$ ) and cathodic ( $i_c$ ) components of the current.

$$i = i_c - i_a \quad (6)$$

The anodic and cathodic components can be expressed as

$$i_a = F A k_b C_R(0, t) \quad (7)$$

$$i_c = F A k_f C_O(0, t) \quad (8)$$

where  $A$  is the area of the electrode, and  $C_R(x, t)$  and  $C_O(x, t)$  are the concentrations of the reduced and oxidized species at  $x$  distance from the electrode surface at time,  $t$ . For an electrochemical cell at equilibrium, the net current is zero, thus  $i_c = i_a = i_0$ , which can be expressed as

$$i_0 = F A k_0 C_O^* e^{-\alpha f (E_{eq} - E^{0'})} \quad (9)$$

where  $k_0$  is the standard rate constant,  $C_O^*$  is the concentration of the oxidized species in the bulk solution,  $\alpha$  is the transfer coefficient, and  $f = F/RT$ , where  $R$  is the gas constant and  $T$  is the temperature. Since the system is at equilibrium,

$$e^{-\alpha f (E_{eq} - E^{0'})} = \left( \frac{C_O^*}{C_R^*} \right)^{-\alpha} \quad (10)$$

Substituting (23) into (9) results in

$$i_0 = F A k_0 C_O^{*(1-\alpha)} C_R^{*\alpha} \quad (11)$$

Combining (6)-(9), dividing (11), and rearranging gives the current-overpotential equation

$$i = i_0 \left[ \frac{C_O(0, t)}{C_O^*} e^{-\alpha f \eta} - \frac{C_R(0, t)}{C_R^*} e^{(1-\alpha) f \eta} \right] \quad (12)$$

which relates the Faradaic current to the applied potential and allows us to begin investigating the kinetics of the redox chemistry taking place in the electrochemical cell.

If we consider the case of a well-stirred solution, or a solution with very low current flowing through the cell, such that the concentration of the redox species at the surface of the electrode is equal to the concentration of the redox species in the bulk solution, (12) reduces to

$$i = i_0 [e^{-\alpha f \eta} - e^{(1-\alpha) f \eta}] \quad (13)$$

which is known as the *Butler-Volmer equation*. Both Equations (12) and (13) can be used to probe the kinetics of the reaction at the electrode-electrolyte interface. However, the observed current is frequently different from the predicted current due to *non-Faradaic* processes occurring at the electrode surface. Slight changes in the composition of the electrolyte solution, applied potential, adsorption or desorption of contaminating species, or the reactions of impurities in the solution or in the metal of the electrode itself contribute to the net current flowing through the electrochemical system. In the next section, the nature of the electrode-electrolyte interface is discussed.

## 1.2. The Electrical Double Layer

Thus far, electrochemistry has been discussed in terms of thermodynamics and kinetics to introduce electrode potentials, charge transfer, and the general workings of a three-electrode setup. In this section, the electrode-electrolyte interface is examined more closely, particularly as it relates to charge separation and capacitance. If we consider an electrode with a negative charge, as in **Figure 2**, we can see that several 'layers' of ions are at the electrode surface when it is placed into an aqueous electrolyte solution.<sup>1,5,6</sup> The first layer, which is called the *Stern layer*, within the *Inner Helmholtz Plane* (IHP), consists of solvent molecules and unsolvated or partially solvated ions of the opposite charge to that of the electrode. These solvent molecules and ions are said to be *specifically adsorbed* to the surface of the electrode, meaning that if the electrode or surrounding electrolyte solution were moved, the ions would remain fixed to the electrode surface. The charge density of these ions is  $\sigma^i$  ( $\mu\text{C}/\text{cm}^2$ ). The second, *diffuse layer*, extending

from the IHP through the *slipping plane* or *Outer Helmholtz Plane* (OHP) to the bulk solution, consists primarily of ions of the same charge as the first layer. However, unlike the inner layer, these ions are solvated and *non-specifically adsorbed*, meaning they have some freedom of movement due to electrostatic repulsion and lower spatial restrictions. The charge density of these ions, which extends from the OHP to the bulk solution, is  $\sigma^d$ . Together, these charge densities sum to give the charge density in the electrolyte solution,  $\sigma^S$ , which is equal but opposite to that of the charge density of the metal electrode,  $\sigma^M$ , by Equation (14)

$$\sigma^S = \sigma^i + \sigma^d = -\sigma^M \quad (14)$$

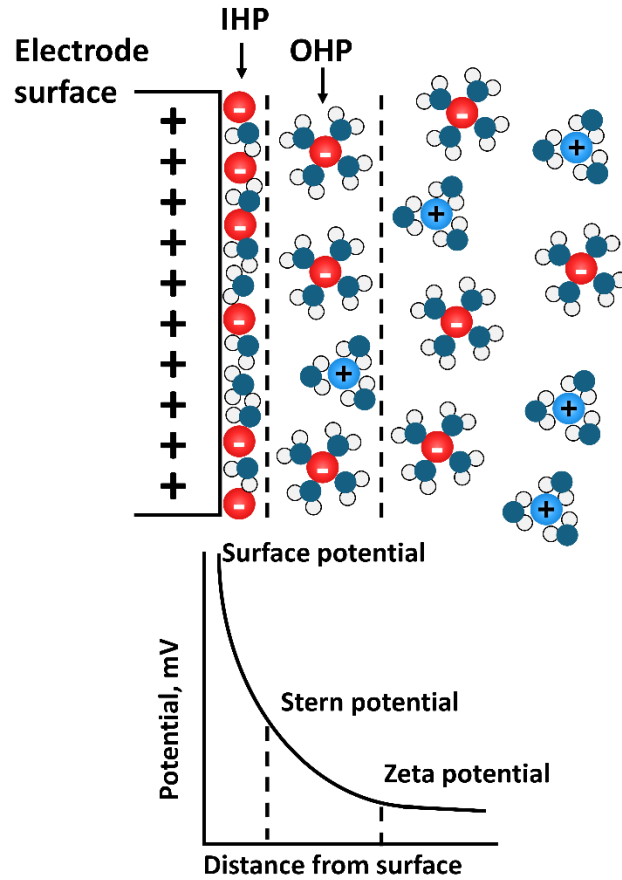


**Figure 2:** Model of the electrical double layer at the electrode-electrolyte interface and the corresponding potential as a function of distance from the electrode surface.

The charge density of the metal electrode,  $\sigma^M$ , is related to the electric field strength by Equation (15)

$$\sigma^M = (8k_B T \epsilon \epsilon_0 n^0)^{1/2} \sinh\left(\frac{ze\phi_0}{2k_B T}\right) \quad (15)$$

For a system with a compact double layer, the field strength at a distance  $x = x_2 = \text{OHP}$  from the electrode surface can be taken as

$$\left(\frac{d\phi}{dx}\right)_{x=x_2} = \left(\frac{8k_B T n^0}{\epsilon \epsilon_0}\right)^{1/2} \sinh\left(\frac{ze\phi_0}{2k_B T}\right) \quad (16)$$

However, this field strength only holds true for a compact double layer, where the electrolyte concentration is high, so the electric field is linear throughout the double layer. If we consider a solution with a low concentration of supporting electrolyte, where the double layer is larger, we can calculate  $\phi_0$  as a total potential drop across the double layer.

$$\phi_0 = \phi_2 - \left(\frac{d\phi}{dx}\right)_{x=x_2} \quad (17)$$

Differentiation and rearrangement gives

$$\left(\frac{d\sigma^M}{d\phi_0}\right)_{x=x_2} = C_d \quad (18)$$

where  $C_d$  is the total capacitance of the double layer, expressed as

$$\frac{1}{C_d} = \frac{1}{C_H} + \frac{1}{C_D} \quad (19)$$

where  $C_H$  is the capacitance of the OHP and  $C_D$  is the capacitance of the diffuse layer. Simply put, capacitance is the ability of a material to store an electric charge. For an electrode with applied potential,  $E$ , charge will accumulate at the surface of the electrode until the charge,  $Q$ , satisfies Equation (20).

$$\frac{Q}{E} = C \quad (20)$$

As a result of this charging process, a charging current will flow through the electrochemical system, which decays exponentially with time, according to Equation (21).

$$i = \frac{E}{R_s} e^{-t/R_s C_d} \quad (21)$$

To round out this section, a brief introduction to *zeta potential* is necessary. The zeta potential is the potential difference at the *slipping plane* between the non-specifically adsorbed layer and the bulk solution, as discussed in 2.3.2.<sup>6</sup> The theory of the double layer can also be extended to particles in solution, as we will see in later sections.

### 1.3. Mass Transport Mechanisms

With the understanding of the general electrochemical cell and the electrical double layer, we can now consider what influences the movement of material from one location to another. In electrochemistry, this process is collectively known as mass transport.<sup>1,7</sup> There are three types of mass transport: diffusion, convection, and migration, which can be described by the *Nernst-Planck equation*.

$$J_i(x) = -D_i \frac{\delta C_i}{\delta x} - \frac{z_j F}{RT} D_j C_j \frac{\delta \phi(x)}{\delta x} + C_j v(x) \quad (22)$$

The simplest, which has already been alluded to in previous sections, is diffusion, which is defined as the movement of a species in response to a concentration gradient and can be described by Fick's first law as the first term from Equation (22).

$$J_i = -D_i \frac{\delta C_i}{\delta x} \quad (23)$$

where  $J_i$  is the flux of species  $i$  per unit time across a given segment,  $\delta C_i$  is the concentration gradient, and  $D_i$  is the diffusion coefficient ( $cm^2/s$ ). The negative sign arises from the direction of the flux opposing the increasing electrochemical potential. If we again consider Equation (1), where a negative charge is being applied to the electrode, reducing  $O \rightarrow R$ , we can see that the decrease in  $O$  at the electrode surface generates a concentration gradient near the electrode surface. This depletion zone, where  $C_O \neq C_O^*$ , is termed the *diffusion layer*. Equation (23) only holds true, however, if the movement of  $C_O$  and  $C_R$  remains constant. *Fick's second law* provides more experimentally meaningful insight,<sup>8</sup>

$$\frac{\delta C_O(x, t)}{\delta t} = D_O \left( \frac{\delta^2 C_O(x, t)}{\delta x^2} \right) \quad (24)$$

which shows the distance a particle can move per unit time. This random, Brownian movement leads to the calculation of the diffusion coefficient, which provides insight into the nature of the species. To obtain a relationship between the diffusion-controlled current over time, we apply the following boundary conditions to Equation (24),

$$t = 0, \quad \text{all } x, \quad C_O = C_O^*$$

$$t > 0, \quad x = 0, \quad C_O = 0$$

$$t > 0, \quad x \rightarrow \infty, \quad C_O = C_O^*$$

we can derive the Cottrell equation,<sup>9</sup>

$$i(t) = \frac{nFA\sqrt{D_O C_O^*}}{\sqrt{\pi t}} \quad (25)$$

which shows the inverse square-root decay of current,  $i$ , with time,  $t$ . This inverse relationship is due to the growth of the diffusion layer thickness over time, though it rapidly reaches a maximum thickness of  $6\sqrt{D_0 t}$  from the electrode surface. If we consider a disk ultramicroelectrode (UME), which is an electrode with a radius of  $r_e = 25 \mu\text{m}$  or less<sup>8,10</sup> as in **Figure 3**, we can see that the original three boundary conditions, now in two dimensions to account for both radial (along the  $r$  axis) and normal (along the  $z$  axis) diffusion to the electrode surface,<sup>11</sup> and two additional boundary conditions are needed for (24). The additional boundary conditions reflect that redox does not occur at the sheath surrounding the electrode surface and the concentration of the oxidized species is zero after time  $t = 0$  for a large potential step. All boundary conditions are summarized below:

$$t = 0, \quad C_O(r, z, 0) = C_O^*$$

$$t > 0, \quad r \rightarrow \infty, \quad C_O = C_O^*$$

$$t > 0, \quad z \rightarrow \infty, \quad C_O = C_O^*$$

$$r > r_e, \quad \left. \frac{\delta C_O(r, z, t)}{\delta z} \right|_{z=0} = 0$$

$$t > 0, \quad r \leq r_e, \quad C_O(r, 0, t) = 0, \quad C_O = C_O^*$$

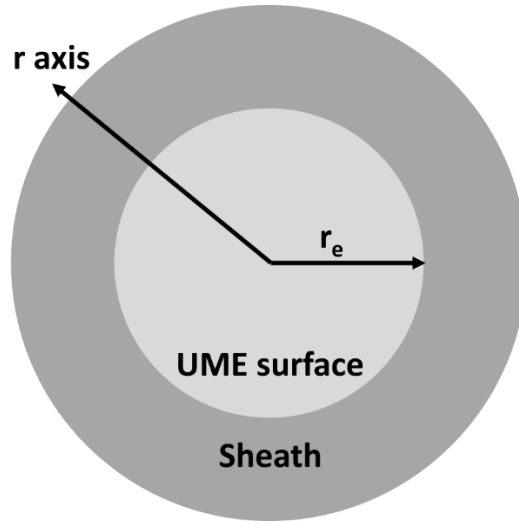


**Figure 3:** Geometry of the surface of an ultramicroelectrode, with radius  $r_e \leq 25 \mu\text{m} \leq r$ , surrounded by a non-electroactive sheath.

Applying the above boundary conditions to the Cottrell equation yields the *steady-state* equation of a disk UME,

$$i_{ss} = 4nFD_0C_0^*r_e \quad (26)$$

which readily relates the steady-state current observed for a disk UME to the radius of the electrode,<sup>1,12</sup> the diffusion coefficient of the redox species, and the concentration of the redox species, which will be of use in the later discussion of cyclic voltammetry at UMEs.

The second type of mass transport, represented by the second term in Equation (22) is migration, which is movement of a species in response to a potential gradient. Recalling the electrical double layer present at the electrode surface, the current due to migration for ionic species  $j$  is:

$$i_j = \frac{z_j^2 F^2 A D_j C_j}{RT} \cdot \frac{\delta\phi}{\delta x} \quad (27)$$

Using the Einstein-Smoluchowski equation, we can see that the mobility of species  $j$  is related to the diffusion coefficient,

$$\mu_j = \frac{|z_j|FD_j}{RT} \quad (28)$$

which allows us to simplify Equation (27) to

$$i_j = |z_j|FA\mu_jC_j \frac{\delta\phi}{\delta x} \quad (29)$$

The total current in the bulk solution is given by

$$i = \sum_j i_j \quad (30)$$

The fraction of the current carried by  $j$  is called the transport number,  $t_j$ . Dividing (29) by (30) yields:

$$t_j = \frac{i_j}{i} = \frac{|z_j|\mu_jC_j}{\sum_k |z_k|\mu_kC_k} \quad (31)$$

The third type of mass transport, represented by the third term in Equation (22) is convection, which is movement of a species in response to movement of the surrounding solution. Convection can be further broken into two types: *forced* convection, which arises from stirring the solution, and *natural* convection, which arises from density gradients in the solution. Density gradients arise at the electrode surface from differing densities between the oxidized and reduced species, or from heat generated by the redox process at the electrode surface. Convection is generally

eliminated in electrochemical experiments, including the ones carried out in this work, by not stirring the solution and minimizing vibrations to facilitate less rigorous calculations.

## 1.4. Cyclic Voltammetry

Thus far, electrochemistry has been discussed as a static process at an electrode, occurring at a constant applied potential over time. In this section, we begin to discuss electrochemistry in terms of a series of redox processes occurring as a function of a changing applied potential. We begin with the simpler example of cyclic voltammetry at a macroelectrode, then move on to discuss the slightly more complex case of cyclic voltammetry at an ultramicroelectrode.

### 1.4.1. Cyclic Voltammetry at Macroelectrodes

To facilitate a complete understanding of cyclic voltammetry, we will first explore the technique as it is performed with disk macroelectrodes, which only experience planar diffusion. The large surface area of the macroelectrode leads to the semi-infinite linear diffusion profile seen in the earlier discussion of diffusion. First, we will consider a three-electrode setup placed in an aqueous redox solution with a high electrolyte concentration. For simplicity, we will assume the redox couple is potassium ferrocyanide ( $\text{K}_4[\text{Fe}(\text{CN})_6]$ ) being oxidized to potassium ferricyanide ( $\text{K}_3[\text{Fe}(\text{CN})_6]$ ). At first, the potential applied to the working electrode is such that no charge transfer (or only non-Faradaic reactions) occurs.<sup>1,13</sup> Then the applied potential is linearly swept at a constant rate (mV/s) from the initial potential,  $E_1$ , to a potential well past where oxidation occurs. As the potential approaches the standard potential,  $E^0$ , of the redox couple, charge transfer begins and current begins to flow.

With each step increase of the potential, new Faradaic processes and double-layer charging occurs, contributing to the total current being measured through the working electrode until it reaches a maximum peak current,  $i_p$ . As the concentration of ferrocyanide near the surface of the electrode is depleted and the applied potential moves past  $E^0$  to the final potential,  $E_2$ , the

current begins to decrease, and the diffusion-limited current is reached. The potential is then swept back to the initial potential at the same rate. As the potential sweeps back through  $E^0$  toward  $E_1$ , the ferricyanide that built up at the electrode surface begins to reduce back to ferrocyanide, eventually depleting itself as the potential returns to  $E_1$ . For a reversible redox process at a macroelectrode as described above, the resultant cyclic voltammogram (CV) generally looks like that shown in **Figure 4**.

By the Randles-Sevick equation, the peak current,  $i_p$ , is directly proportional to the square root of the scan rate.

$$i_p = 0.4463nFAC^0 \left( \frac{nFvD_0}{RT} \right)^{1/2} \quad (32)$$

Thus, for higher scan rates, a higher peak current is observed. The Randles-Sevick equation takes the form of the point slope equation, allowing the area of an electrode, the diffusion coefficient, or the number of electrons transferred to be determined experimentally for increasing scan rates.

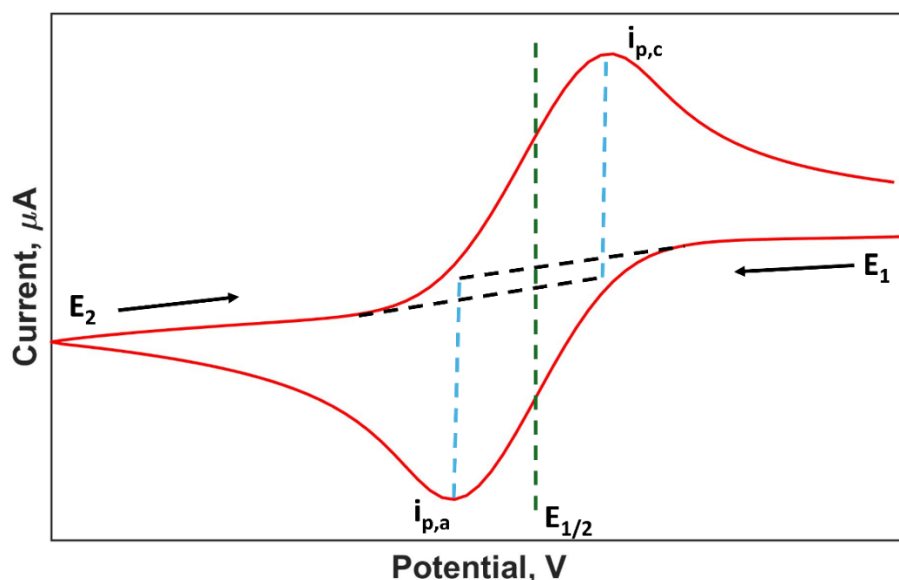


**Figure 4:** General cyclic voltammogram of a reversible redox reaction occurring in an aqueous solution with a high electrolyte concentration at a macroelectrode. The potential is changed at a constant rate from  $E_1$  to  $E_2$ , then back to  $E_1$ . It should be noted that by U.S. convention, low potentials are to the right of the x-axis and high potentials are to the left of the x-axis.

At the potential directly between the peak currents, the concentrations of both the oxidized and reduced species are approximately equal. Following the Nernst equation, the *half-wave potential* is approximately equal to the standard potential.

$$E = E^0 + \frac{RT}{nF} \ln \frac{C_O}{C_R} \quad (33)$$

From above, we can see that much can be learned from a CV of an ultramicroelectrode. In the next section, cyclic voltammetry at an ultramicroelectrode is considered.

### 1.4.2. Cyclic Voltammetry at Ultramicroelectrodes

As previously discussed, disk ultramicroelectrodes (UMEs) represent miniaturized electrodes utilized in electrochemistry, enabling low potentiostatic currents and expanding the realm of

electrochemical detection to single particles. Typically, disk UMEs have a diameter of 50  $\mu\text{m}$  or less and are fabricated by sealing a metal wire into a capillary composed of an electrochemically inert material, such as glass or resin. After sealing the capillary, a cross section of the wire is exposed by cutting or sanding, then the electrode surface is polished to a mirror finish. The meticulous fabrication process ensures precise control over the electrode dimensions and surface characteristics, which are essential for reliable electrochemical measurements. While commercial UMEs are available, many laboratories opt to fabricate their own UMEs for increased control over the electrode characteristics.

Expanding on the concept of radial and normal diffusion first discussed in Section 1.3., when a sufficient potential to facilitate charge transfer is applied to the electrode surface, the current density is non-uniform across its face due to diffusion occurring in two dimensions: radially towards the edges of the electrode, and normally, or perpendicularly, to the electrode surface. This non-uniform distribution of current density can significantly influence the performance of UMEs in their various applications, highlighting the importance of understanding mass transport phenomena.

**Figure 5a** illustrates both dimensions of diffusion as a redox species approaches the surface of an UME, thereby creating the diffusion profile depicted from above the surface of the UME surface

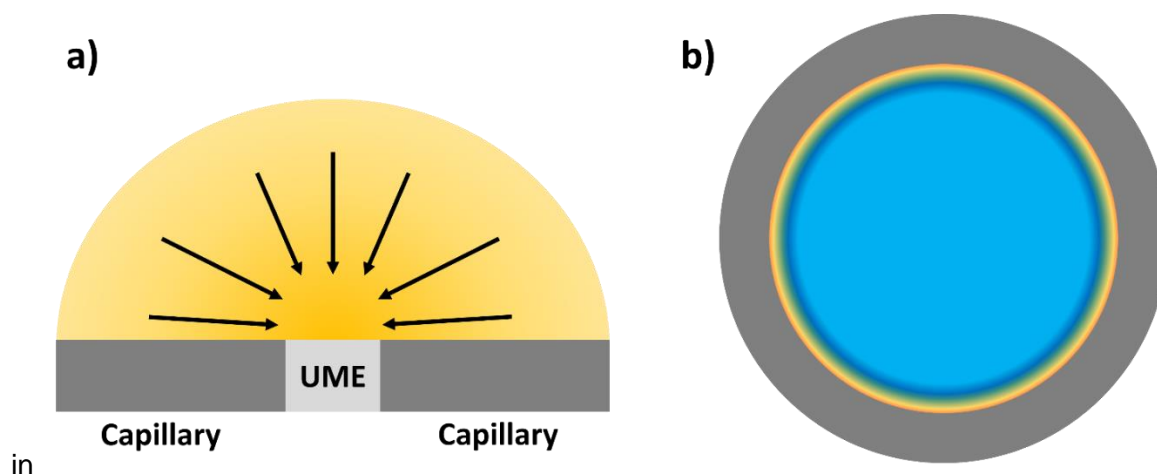


Figure 5b.

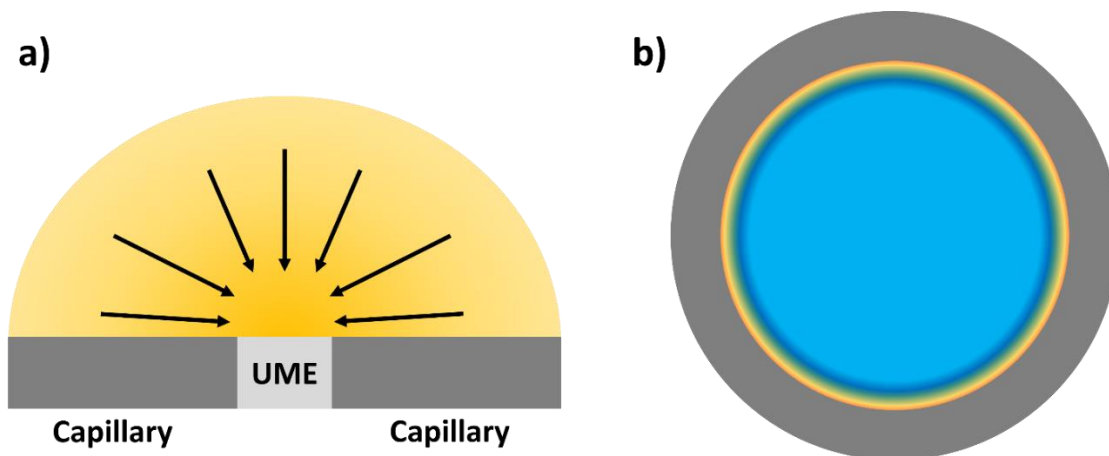
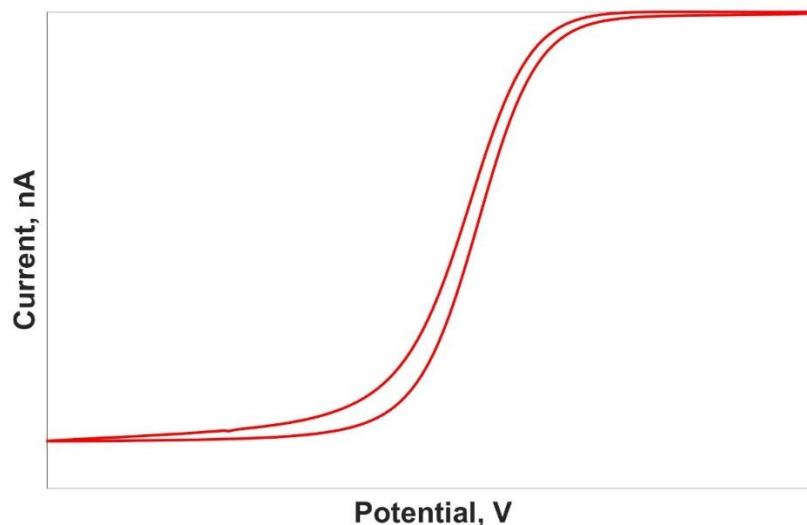


Figure 5. Diffusion profile of a disk ultramicroelectrode a) from the side and b) from above.

For a potential sweep performed at an ultramicroelectrode, the 'duck shape' observed with the macroelectrode flattens, resulting in a more 'S-shaped', or *sigmoidal* CV,<sup>1,10,13</sup> which is shown in **Figure 6**. As discussed in Section 1.3., the diffusion-limited current can be calculated by Equation (26). Unlike in the case of the macroelectrode, the steady-state current is theoretically independent of the scan rate, which experimentally holds true for small scan rates. In this section, cyclic voltammetry and its uses have been briefly discussed to provide insight into the experimental results presented later in this work.



**Figure 6:** Generic cyclic voltammogram of a reversible redox reaction occurring in an aqueous solution with a high electrolyte concentration at an UME. Working electrode: Pt UME vs 3 M Ag/AgCl reference electrode. Scan rate 50 mV/s.

## 1.5. Chronoamperometry

Here, the primary electrochemical method used in the rest of this work is introduced. Contrary to cyclic voltammetry, where the potential is stepped at a constant rate, a large potential step is introduced to the electrochemical cell, such that the steady-state current, for a UME, is reached shortly after the potential step is applied.<sup>1</sup> The desired potential is generally selected to be within the region of the steady-state current, obtained from the CV of the solution. Selecting a potential before the steady-state current is reached will result in a chronoamperogram, or *i-t curve*, that is not diffusion-limited and thus does not follow Equation (26). On the other hand, selecting a potential too far into the steady-state region can increase the contribution of the non-Faradaic current as additional undesired processes occur at the electrode surface as a result of the increased energy introduced into the system. Generally, selecting a potential 1-2 mV into the steady-state region is standard and this potential is called the *steady-state potential*.

Immediately following application of the steady-state potential, the charging current forms the double layer at the electrode surface. While the diffusion layer thickness is small at short experimental times, the current decays according to the Cottrell equation (Equation (25)). At longer experimental times, as the diffusion layer thickness grows, the current plateaus according to the equation for the steady-state current (Equation (26)). The steady-state current provides an excellent background to measure the interactions of particles with the electrode, which will be introduced in the next chapter.

# Chapter 2

## Fundamentals of Single-Entity Electrochemistry and Other Important Principles

This chapter provides an in-depth review of the field of single-entity electrochemistry, particularly as it pertains to insulating particles like bacteria. Bacteria are of significant interest in clinical healthcare as illnesses caused by antibiotic-resistant bacteria result in an increasing number of deaths each year. While working to expand the theoretical understanding of the world at the nanoscale is important, it is necessary to develop techniques to advance the field of bacterial sensing at the single cell level. Generally, diagnostic methods to identify bacterial infections rely on waiting for the bacteria to grow, often overnight, until a colony of the bacteria can be observed. Work in the field of single-entity electrochemistry has demonstrated that single bacterial cells can be detected at the femtomolar level. The signals produced by single bacteria in the same sample have been shown to vary as a function of the bacteria's size, surface properties, and its environment. As such, developing a method that allows characterization of individual bacteria, rather than an ensemble, would allow for improved diagnostics in clinical settings. Further, antibiotic-resistant bacteria arise as bacteria treated with antibiotics develop a resistance to the antibiotic. Improving our understanding of the cellular changes produced by antibiotics in individual cells over time will allow healthcare providers to provide rapid, targeted treatment and pharmaceutical companies to develop new antibiotics.

To study bacteria electrochemically, the size of the working electrode must be of similar size to the analyte. As discussed in the previous chapter, ultramicroelectrodes offer this advantage, and additionally offer low noise, facilitating sensitive measurements of nanoparticles. Previous work has shown that bacteria can be detected in many redox solutions and produce different types of signals depending on the identity of the redox species and the concentration of the supporting electrolyte, which is primarily discussed in this chapter. Relevant methods, such as dynamic light

scattering (DLS) and zeta potential, which add depth to the electrochemical experiments, are also introduced.

## 2.1. Insulating Particles

Insulating particles are non-conducting entities that range from a few nm to a few  $\mu\text{m}$  in size.<sup>14</sup> Of particular interest in this dissertation are *Aeromicrobium erythreum* and *Bacillus subtilis*, two gram-positive bacteria isolated from soil.<sup>15,16</sup> Before the discovery of bacteria by Antony van Leeuwenhoek in 1677<sup>17</sup>, the prevailing theory behind the spread of disease was miasma, or ‘bad air’ in the environment causing ill effects on the human body.<sup>18</sup> The next momentous discovery in understanding disease came almost 200 years later in the 1860s when Louis Pasteur created the first liquid culture medium and proved that microorganisms do not spontaneously generate.<sup>18,19</sup> Around the same time, Robert Koch created the first solid culture medium and proved that particular bacteria cause specific diseases. These discoveries birthed the field of microbiology and paved the way for the discovery of antibiotics, the structure of DNA, and gene sequencing.<sup>18,20</sup>

In the almost two centuries since Koch’s and Pasteur’s discoveries, plate culturing has been the gold standard for diagnosing bacterial infections.<sup>21</sup> However, in the age of antibiotic-resistant bacteria, novel methods to facilitate faster detection and identification of bacteria is critical. In 1985, the polymerase chain reaction technique was developed as an alternative to plate culturing, which has since grown to encompass a series of techniques focusing on faster identification of bacterial cells.<sup>22</sup> Single-entity electrochemistry, with its low detection limits, high selectivity, and short experimental time, offers a tantalizing next step in clinical biosensors.

Single-entity electrochemistry is an electrochemical technique that allows for the detection of single particles, within an ensemble. The technique was first reported in a pivotal article by Quinn, van’t Hoff, and Lemay in 2004,<sup>23</sup> wherein single, insulating carboxylated latex beads were detected at a Au ultramicroelectrode. Since the initial report two decades ago, a myriad of

insulating biotargets, including proteins, viruses, bacteria, red blood cells, and yeast, have been investigated by single-entity electrochemistry experiments.<sup>24–28</sup> With the increased ability to separate the individual response from the ensemble, there has been a focus on understanding and controlling the behavior of many different types of micro- and nanoparticles as they interact with the surface of an ultramicroelectrode (UME).

## 2.2. Single-Entity Electrochemistry

### 2.2.1. Types of Signals

Single-entity electrochemistry can generally be broken into two types of experiments: those in which current is increased, and those in which current is decreased, as shown in **Figure 7**.<sup>29</sup> In both types of experiments, a steady-state potential is applied to the working electrode and the current is monitored over time. As particles interact with the electrode surface, the current is transiently increased or decreased, depending on the nature of the particle. For an insulating particle of  $\sim 1\ \mu\text{m}$  in a redox solution that approaches a biased  $10\ \mu\text{m}$  diameter electrode through diffusion, as in **Figure 7A**, two outcomes are possible. First, the particle could adsorb to the electrode surface, locally blocking the diffusive flux through the electrode and creating a step-like transient in the  $i$ - $t$  curve.<sup>30,31</sup> If the particle does not adsorb to the electrode and instead bounces off, the diffusive flux will be temporarily blocked, resulting in a spike-like transient in the  $i$ - $t$  curve. Over time, this method has become known as “blocking electrochemistry”. Due to the non-homogenous flux at the surface of ultramicroelectrodes, it is difficult to relate the magnitude of the current change with the size of the insulating particle – for instance, a particle will produce a larger change in current when it lands at the edge of the electrode than when it lands in the center of the electrode, a phenomena known as the ‘edge effect’.<sup>26</sup>

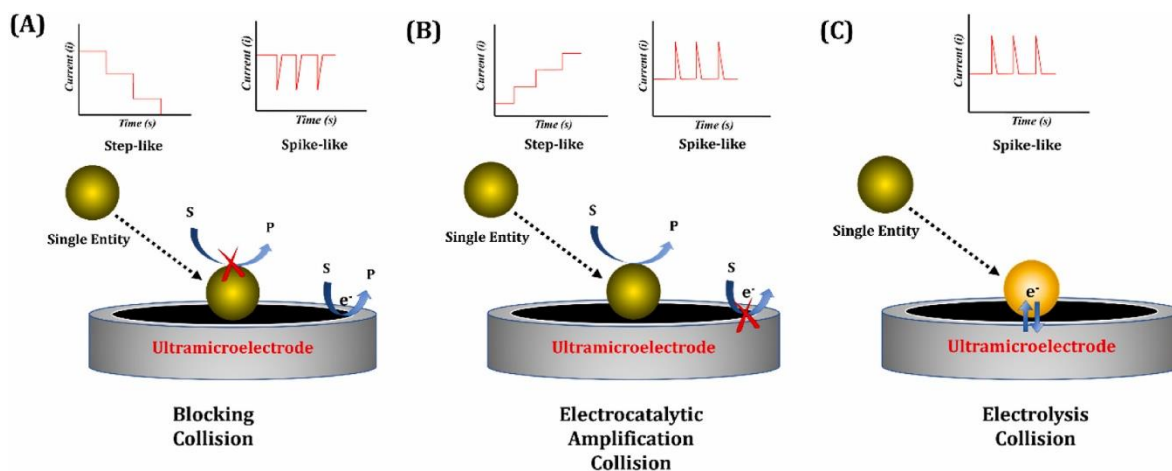


**Figure 7:** The primary types of collisions seen in single-entity electrochemistry experiments. A) Collisions of insulating particles that block, or decrease, the observed signal in an  $i-t$  curve. B) Collisions of conducting particles that generate, or increase, the observed signal in an  $i-t$  curve. C) Collision of a non-conducting particle that increases the observed signal in an  $i-t$  curve. Reprinted with permission from reference (29).

For a conducting particle of  $\sim 1 \mu\text{m}$  in a redox solution that approaches the same electrode through diffusion, as in **Figure 7B**, two similar outcomes are possible. The particle could adsorb to the electrode, facilitating charge transfer and acting as a miniature electrode, thus generating current and creating a step-like transient in the  $i-t$  curve. Alternatively, the particle could bounce off the electrode surface, briefly catalyzing redox and creating a spike-like transient in the  $i-t$  curve.

For the final case in **Figure 7C**, the particle itself acts as the redox molecule or is a droplet containing the redox molecule.<sup>32,33</sup> Here, we will consider the case of an aqueous,  $\sim 1 \mu\text{m}$  droplet in an containing redox species dispersed in an organic solvent. Upon reaching the electrode surface, charge transfer from the redox species to the electrode occurs, generating current flow. Due to the small size of the droplet, the redox species is quickly depleted, restoring the current to its baseline.

Much information can be learned about the particles from the transients observed in their respective  $i-t$  curves. Under diffusion-controlled conditions, the steady state equation can be converted to

$$f = 4N_A C_p^* D_p r_e \quad (34)$$

where  $f$  is the collisional frequency,  $N_A$  is Avogadro's number,  $C_{redox}^*$  is the bulk concentration of the particle,  $D_p$  is the diffusional coefficient of the particle, which can be calculated by the Einstein relation<sup>34</sup> (Equation (35)), and  $r_e$  is the radius of the electrode.

$$D = \frac{k_B T}{6\pi\eta r_p} \quad (35)$$

Where  $k_B$  is Boltzmann's constant,  $\eta$  is the fluid viscosity, and  $r_p$  is the particle radius. For emulsion droplets, the transient signals can be integrated to calculate to the total charge passed,

$$dQ = di \cdot dt \quad (36)$$

where  $dt$  is the total time of the transient signal. By simple unit analysis, the charge can be converted to the volume of the droplet.

$$V = \frac{4}{3}\pi r^3 = \frac{Q}{nFC_{redox}^*} \quad (37)$$

Rearranging leads to the droplet diameter,  $d$ .

$$d = \sqrt[3]{\frac{6Q}{n\pi F C_{redox}^*}} \quad (38)$$

Thus, single-entity electrochemistry offers insight into the properties of micro- and nanoparticles within a bulk solution. Bacteria present a unique challenge, as they are generally not perfectly round, and their diffusion coefficient cannot be readily calculated by Equation (35). As will be seen in future chapters, this work focuses on expanding single-entity electrochemistry to the characterization and identification of rod-shaped bacteria.

### **2.2.2. Recent Advances in Blocking Electrochemistry**

While the focus of this work is on the interactions of bacterial cells on the surface of an ultramicroelectrode, work performed with all types of insulating particles can provide many useful insights. In the initial work published in 2004, Quinn, van't Hoff, and Lemay demonstrated the first use of single-entity electrochemistry to amperometrically detect insulating latex micro- and nano-beads at the surface of a Au ultramicroelectrode.<sup>23</sup> As the beads adsorbed to the electrode surface, they blocked the local flux of the redox species at that location, resulting in a step-like decrease in signal. By placing the beads in high concentrations of electrolyte with their redox species, ferrocenemethanol, they demonstrated that the adsorption frequency was quite low, ~1 signal per 300 seconds. The low adsorption frequency and high supporting electrolyte concentration supports the conclusion that the beads approached the electrode through diffusion. On the other hand, by placing the beads in low concentrations of electrolyte with ferrocenemethanol, an uncountable number of steps (as the beads completely covered the electrode surface) was observed per 300 seconds. The large adsorption frequency, coupled with the low supporting electrolyte concentration, supports the conclusion that the beads approached the electrode by migration. From these experiments, it was shown that insulating particles could be detected at the surface of an ultramicroelectrode, and their mass transport could be controlled by manipulation of the supporting electrolyte concentration. Later work by Bard *et al.* expanded on this by detecting 310 nm silica spheres adsorbing to the surface of a 2  $\mu\text{m}$  Pt ultramicroelectrode (+0.5 V vs Ag/AgCl) at different electrolyte concentrations.<sup>35</sup> At low supporting

electrolyte concentrations, an adsorption frequency of 0.075 Hz was observed, which was significantly higher than the calculated diffusional adsorption frequency, supporting the conclusion that the beads were approaching the electrode by migration. The assumption of migration was further supported by the negative zeta potential of the beads resulting in electrostatic attraction to the positively charged electrode. In addition to quantifying the frequency and mass transport mechanism, the group used COMSOL Multiphysics to show that the magnitude of the current step is largely influenced by the landing position of the bead, as shown in **Figure 8**. Due to the diffusion profile of a disk ultramicroelectrode, discussed in **Section 1.4.2.**, particles landing at the edge of the electrode block a greater amount of flux, resulting in a greater decrease in current upon particle adsorption.

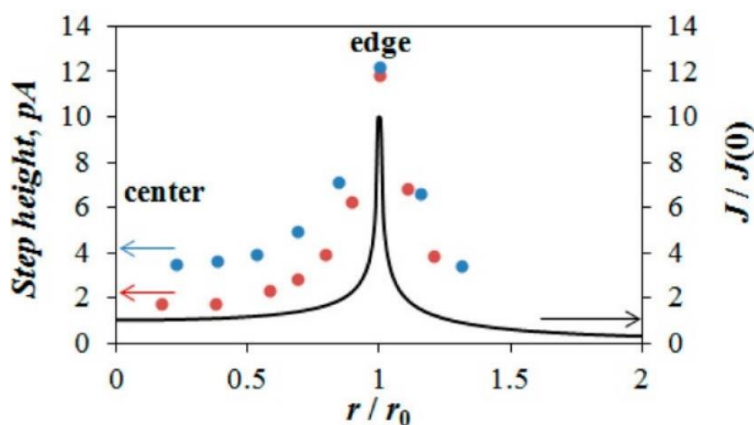


**Figure 8:** Simulated magnitude of blocked current for beads of radius 260 nm, electrode of radius 2.5  $\mu\text{m}$ , and ferrocenemethanol concentration of 2 mM (red dots), and for beads of radius 155 nm, electrode of radius 1  $\mu\text{m}$ , and ferrocenemethanol concentration of 2.5 mM. The black line represents the normalized flux of the redox species through the electrode. Reprinted with permission from reference (35).

In addition to quantifying the magnitude of the current step by landing position, the group also determined how the ratio of the bead radius to electrode radius would affect the magnitude of the current step. As can be seen in **Figure 9**, a larger particle (for particles of the same or smaller

size than the electrode) will produce a larger step than a smaller particle (for a constant landing position). This work highlighted the inherent difficulty in working with disk ultramicroelectrodes as the same particle can produce very different magnitudes of current change.

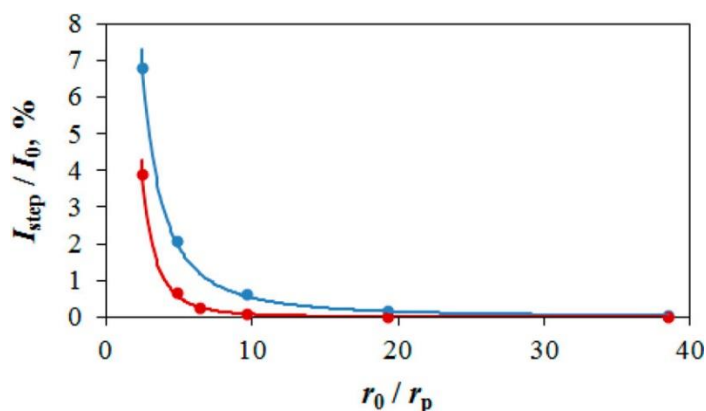


**Figure 9:** Effect of particle size on step magnitude for  $r_0 =$  electrode radius and  $r_p =$  particle radius. Landing positions correspond to the edge of the electrode surface (blue) or electrode center (red). Republished with permission from Reference (35)

In 2016, Lee *et al.* published the first use of blocking electrochemistry using bacteria as an analyte.<sup>36</sup> The group optimized their experimental parameters to ensure that a non-lethal concentration (20 mM) of potassium ferrocyanide was used and determined that a 10  $\mu\text{m}$  diameter carbon fiber electrode would produce the best signal. No supporting electrolyte was used. Step-like signals were observed under these conditions. To confirm the step-like signals were due to *E. coli* adsorption to the electrode surface, the group used fluorescence microscopy to visualize the events bacteria on the surface of the electrode, as seen in **Figure 10**. To confirm that the bacteria moved to the electrode by migration, the group also performed experiments with ruthenium(III) hexamine, which requires the working electrode to be biased negatively. No steps were observed as the negatively charged bacteria were repelled from the electrode surface.

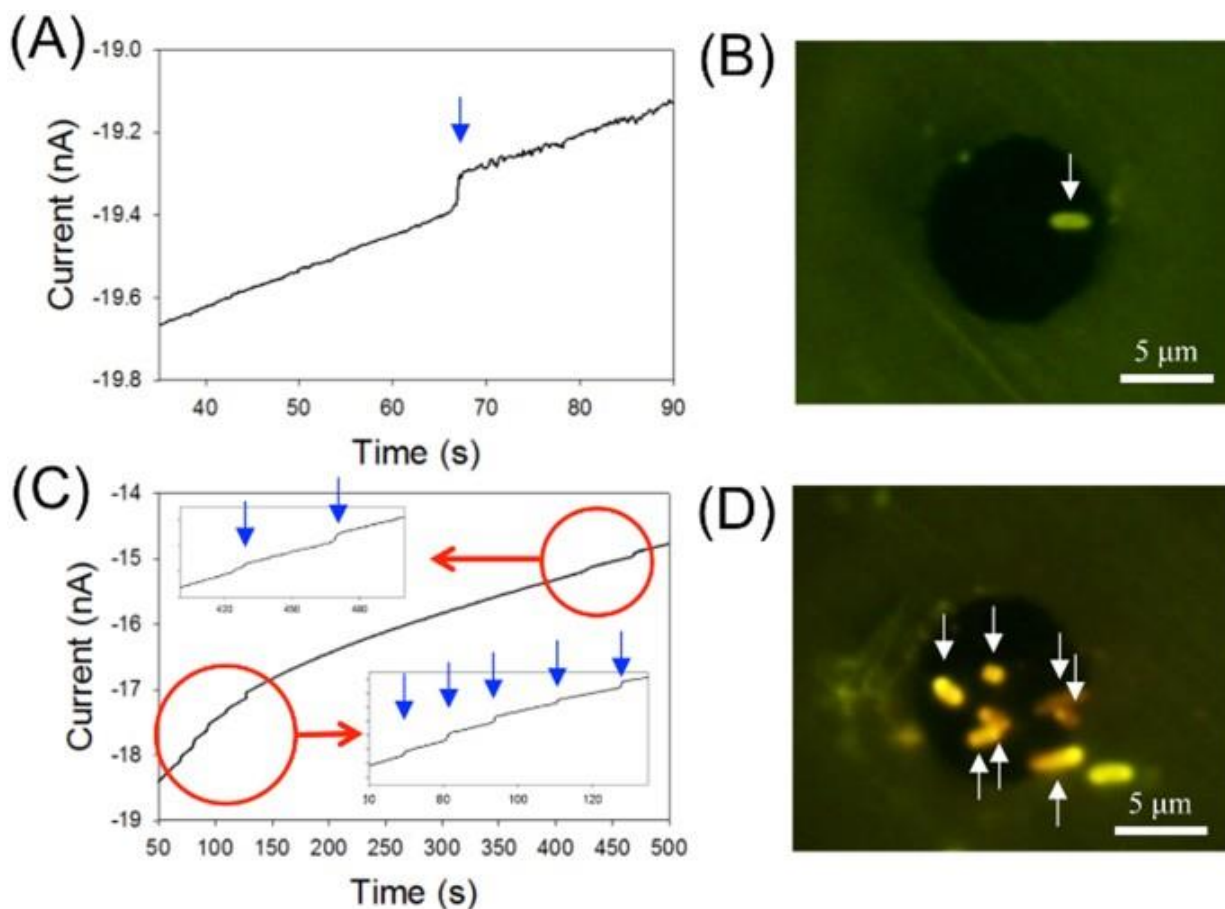


**Figure 10:** (A) A single step observed in a chronoamperogram. (B) A single *E. coli* cell adsorbed to the surface of the electrode after the experiment in (A). (C) Several steps observed in a chronoamperogram. (D) Several *E. coli* cells adsorbed to the surface of the electrode after the experiment in (C).

In addition to experimentally obtained results, Lee *et al.* reported the results of simulations performed in COMSOL for cylindrical cells at landing positions at three different distances from the electrode center. The data was in good agreement with previously reported results, that insulating particles landing nearer to the edge of the electrode will produce a larger current step than a particle landing nearer the electrode center. The experimental magnitude of the current steps was in good agreement with the simulated values. Two years later, Ronspees and Thorgaard reported the detection of *E. coli* and *B. subtilis* by blocking electrochemistry.<sup>37</sup> In 2 mM ferrocenemethanol and 1 mM KCl, at an applied potential of +0.385 V vs Ag/AgCl, the two bacteria

interacted differently with the electrode surface. *E. coli* produced the typical step-like signals observed in previous works, but *B. subtilis* produced primarily spike-like signals, with some step-like signals, as in **Figure 11**. Correlated fluorescence microscopy performed in real-time with the electrochemical experiments revealed that the spike-like signals were due to the *B. subtilis* not adsorbing to, but bouncing off, the electrode surface. This is attributed to the lower magnitude of the zeta potential of *B. subtilis* (-31 mV) compared to *E. coli* (-53 mV), and oxidation of surface moieties mediated by the oxidized ferrocenemethanol. Smaller spike-like signals following *B. subtilis* adsorption events were attributed to movement of one or more of the adsorbed bacterial cells.

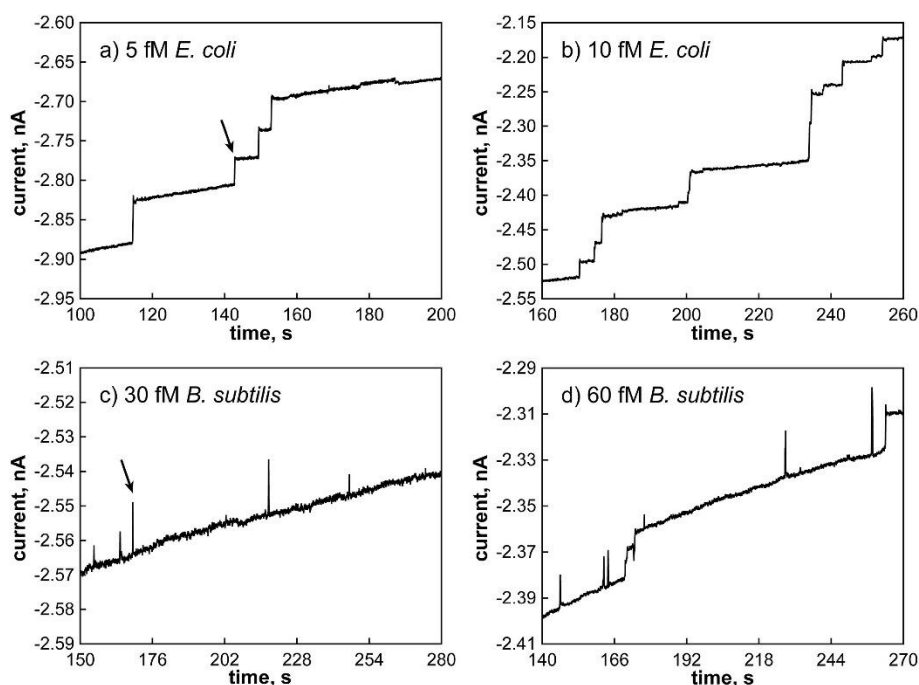


**Figure 11:** a) and b) Step-like signals observed for 5 fM and 10 fM *E. coli*, respectively. c) Spike-like signals observed for 30 fM *B. subtilis*. d) Step- and spike-like signals observed for 60 fM *B. subtilis*. All electrochemical experiments were performed in 2 mM ferrocenemethanol and 1 mM KCl. The 10  $\mu\text{m}$  diameter Pt ultramicroelectrode was biased at +0.385 V vs Ag/AgCl. Reprinted with permission from Reference (37)

That same year, Gao *et al.* published results for the electrochemical detection of *E. coli* and *S. maltophilia* by blocking electrochemistry. The group proposed that the two bacteria could be selectively detected from their activity with the redox species. Further, the signals produced by live bacteria were compared to the signals produced by bacteria exposed to one of two bactericidal agents. Their work demonstrated that bacteria landing on the electrode surface could be detached during the experiment by reversing the potential of the working electrode, then switching back to the original potential, where the current returned to a magnitude greater than was observed at the initial switch. By keeping all parameters the same, except for the identity of the redox species, the group was able to calculate the redox activity of *E. coli* on ferricyanide ( $\text{Fe}(\text{CN})_6^{3-}$ ), wherein steps were not observed in the *i-t* curve. Instead, the number of steps was estimated based on data from an *i-t* curve of *E. coli* in ferrocyanide ( $\text{Fe}(\text{CN})_6^{4-}$ ). As with previous work, they found that the bacteria's size and landing position of the cell on the electrode surface were important factors to the magnitude of the observed signals. To compare the observed signals of positively and negatively charged bacteria, similar blocking experiments were performed with *S. maltophilia*, which has a positive surface charge. As predicted, no signals were observed at a positively-biased electrode and step-like signals were observed in the reduction curve of ferricyanide (-0.4 V vs Ag/AgCl). Interestingly, the steps observed for *S. maltophilia* had a longer duration than those produced by *E. coli* in ferrocyanide. The increased step duration may be due to a lower-magnitude zeta potential, larger size, or the lower-magnitude potential applied to the working electrode.

In addition to the above work, the group exposed *E. coli* to two kinds of antibiotics: colistin, which lyses cells, and cobalt ions, which inhibit cellular respiration. The resultant *i-t* curves show that the cells killed by colistin exhibited an initial sharp decrease in current, followed by a slow increase in current. This is attributed to the speed by which colistin kills cells, allowing them to adsorb to the electrode surface (thereby decreasing the current), then lysing and exposing their redox

centers to the electrode surface, facilitating faster reduction of the oxidized ferrocyanide at the electrode surface, thereby increasing the current. When the cells were killed by cobalt ions, an overall decrease in current was observed, which was attributed to adsorption of the dying cells to the electrode surface. However, the mechanism causing the dying cells to adsorb to the electrode, when they had not done so prior to the addition of the antibiotic, was not discussed. The interesting results presented here bear further scrutiny and are indeed the inspiration for the work presented in this dissertation.

## **2.3. Complementary Methods**

This section focuses on methods that complement the single-entity measurements contained in later sections. Methods include dynamic light scattering, zeta potential, and optical density measurements.

### **2.3.1. Dynamic Light Scattering**

When working with particles that are on the same size scale as the surface area of the working electrode, quantifying the size of the particles is very important. As discussed in Section 2.2., the size of particles can be calculated from the transient signals observed in  $i-t$  curves. However, quantifying the size by another technique can identify gaps between the actual and theoretical sizes. Dynamic light scattering measures the size distribution profile of nanoparticles in a solution by using a laser to examine the light scattering caused by the particles. If the light scattering is monitored over time, the fluctuation of the scattering can be related to the particles movement (by Brownian motion), giving the diffusion coefficient of the particles.<sup>38</sup> From Equation (35), the hydrodynamic radius of the particle can be calculated. As this technique depends on light scattering, it is important the concentration of the analyte be sufficiently low to allow light to pass through the cell.

### 2.3.2. Zeta Potential

For particles being analyzed by single-entity electrochemistry, an understanding of their surface charge is necessary. In Section 1.2., the double layer was introduced as two distinct layers of ions adsorbed to the surface of the electrode: a specifically adsorbed layer and a non-specifically adsorbed layer. This concept of the double layer can be extended to charged particles, as in **Figure 12**. The zeta potential is the charge measured at the slipping plane, which separates the non-specifically adsorbed ions and the bulk solution in the diffuse layer. Knowing the sign and magnitude of zeta potential can provide incredibly useful information, such as the colloidal stability of the particles and how they will interact with a biased electrode. At low magnitudes of zeta potentials, particles will not be sufficiently charged to electrostatically repel each other, which will eventually result in particle aggregation. At higher magnitudes of zeta potentials, particles will electrostatically repel each other, and the analyte will remain homogeneously dispersed in solution. Generally, particles with zeta potentials greater than  $\pm 30$  mV are considered to be stable.

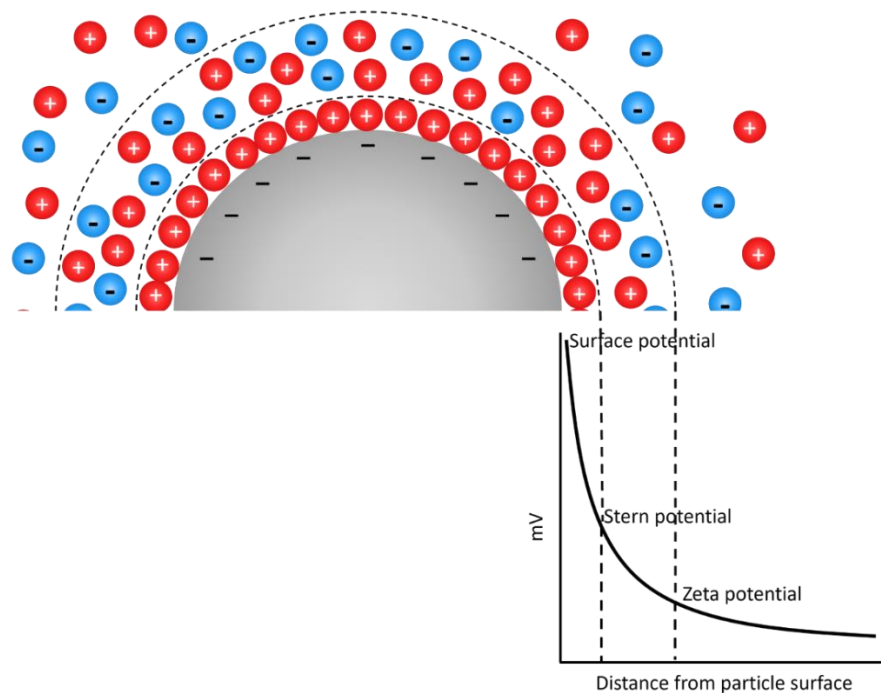


**Figure 12:** Schematic representation of zeta potential, showing the surface potential of a negatively charged particle, the Stern potential at the inner dotted ring (Stern plane), and the zeta potential at the outer dotted ring (slipping plane).

There are two primary factors that affect the zeta potential of a particle in solution: the pH, and the ionic strength of the solution. For a negative particle, as in **Figure 12**, adding acid will increase the size of the double layer and decrease the magnitude of the zeta potential. Conversely, adding base would compact the double layer and increase the magnitude of the zeta potential. This logic can be extended to the concentration of an electrolyte in solution with the negatively charged particle. With more ions in solution, the double layer will compact as the ions surround the particle and grow the double layer.

To measure zeta potential, the solution containing the analyte is placed in a folded capillary cell, which has electrodes on either side. A potential is applied to one electrode (generating a potential at the opposite electrode), creating an electric field. As the particles move toward the electrode they are electrostatically attracted to, their velocity is monitored by laser doppler electrophoresis,

which is a type of dynamic light scattering. This velocity, also called *electrophoretic mobility* ( $\mu_E$ ), allows for the calculation of the zeta potential following Henry's equation.<sup>6</sup>

$$\mu_E = \frac{2\varepsilon\zeta f(\kappa a)}{3\eta} \quad (39)$$

where  $\varepsilon$  is the dielectric constant,  $\zeta$  is the zeta potential,  $f(\kappa a)$  is the Henry function, and  $\eta$  is the solvent viscosity. The Henry function is an approximation of the ratio of the double layer thickness,  $\kappa$ , to the radius of the particle,  $a$ . When the particle is in non-polar media, the Henry function is taken as 1.0 following the Huckel approximation. When the particle is in polar media, the Henry function is taken as 1.5 following the Smoluchowski approximation.

### **2.3.3. UV-vis Spectroscopy**

For bacteria grown in liquid media, the concentration is generally recorded by measuring the  $OD_{600}$ , which is the optical density at 600 nm wavelength. Liquid bacteria cultures are grown by inoculating a nutrient-rich broth with a single colony from an agar plate, then incubating overnight in a rotary shaker at 37°C. An aliquot of the culture is placed in a cell, and the absorbance at 600 nm is recorded. To convert the absorption value to a concentration, a calibration curve correlating concentration to absorption is created for each bacterium. The slope of the calibration curve, within the linear absorption range from 0.5 – 1.5, is the conversion factor used to convert absorption values to concentration.

# Chapter 3

## Electrochemical Detection of Rod-shaped Bacteria by Blocking Electrochemistry

This work expands the field of blocking electrochemistry to include the rod-shaped bacteria, *Aeromicrobium erythreum* and *Bacillus subtilis*. Both bacteria exhibit inhibition of the steady-state current of potassium ferrocyanide at the surface of an ultramicroelectrode (UME), producing “steps” in the chronoamperometric  $i-t$  curve. Under diffusion-controlled conditions, the theoretical and experimental frequency is quantified to determine the potential influence of bacterial self-propulsion.

### 3.1. Introduction

Stochastic blocking electrochemistry has been successfully employed to study a number of insulating particles, including polystyrene beads, bacteria, viruses, proteins, Pt nanoparticles, and emulsion droplets.<sup>23–25,30,31,35,39,40</sup> Due to the random nature of particle movement and rates of diffusion for the particles of interest, relatively long experimental times or high concentrations of analyte are required to obtain a meaningful number of signals in a single experiment. Recent work with charged, spherical insulating has focused on lowering the concentration of electrolyte to grow the electric field at the working electrode, thereby inducing migration of the particles.<sup>41–45</sup> This work expands migration-induced blocking electrochemistry to two rod-shaped bacteria (bacilli), *Aeromicrobium erythreum* and *Bacillus subtilis*.

With the rising threat of antibiotic-resistant bacteria, developing new methods quickly and cost-effectively detect disease-causing bacteria is critical.<sup>46</sup> Blocking electrochemistry has proven that real-time measurements of single, unlabeled bacterial cells is possible.<sup>14,28,31,43,47</sup> Generally, blocking electrochemical experiments are designed so that a working ultramicroelectrode (UME) is biased at a potential such that the analyte will be electrostatically attracted to the electrode

surface, resulting in adsorption of the analyte to the electrode. As the analyte approaches the electrode surface and adsorbs, the flux of the redox species to the electrode surface is locally blocked, resulting in a small net decrease (step) in the steady-state current observed in the  $i-t$  curve. The magnitude of the step can provide valuable information about the size of the blocking entity, and the frequency of the steps observed can provide information about the concentration of the analyte in the bulk solution. Quantitative calculations relating size and concentration values to experimental  $i-t$  curves are complicated by the shape of the bacteria and the geometry of disk UMEs. Due to the diffusion profile of a disk UME, current density is greater at the edges of the electrode surface, resulting in disproportionate step magnitudes for particles of the same size that adsorb to different locations on the UME surface. Further, bacilli do not completely block the electrode surface, as they adsorb on-end, perpendicular to the electrode surface.<sup>47</sup> Herein, the diffusional and migrational interactions of *A. erythreum* and *B. subtilis* with a disk UME are thoroughly characterized.

## **3.2. Experimental**

### **3.2.1. Chemical Reagents**

All reagents were used as received without further purification unless otherwise specified. Potassium hexacyanoferrate(II) trihydrate ( $K_4[Fe(CN)_6]$ , 98.5%), sodium chloride, sodium phosphate dibasic, and potassium phosphate monobasic were obtained from Sigma-Aldrich (St. Louis, MO, USA). Potassium chloride (KCl) was purchased from Thermo Fisher Scientific (Hampton, NH, USA). All aqueous solutions were prepared using Millipore water ( $\geq 18.2 M\Omega \cdot cm$ ) unless otherwise specified.

### **3.2.2. Instrumentation**

All electrochemical experiments were performed using a CHI 660C potentiostat (CH Instruments, Austin, TX, USA) with a three-electrode setup in a single-compartment electrochemical cell

housed in a Faraday cage. The electrode setup was comprised of a 3 M Ag/AgCl reference electrode, Pt wire counter electrode, and a Pt working ultramicroelectrode (UME). Before and between experiments, the Pt UME was gently polished with 0.05  $\mu\text{m}$  alumina powder (Buehler, Lake Bluff, IL, USA) slurry on a Buehler polishing pad. Dynamic light scattering (DLS) experiments were performed using a ZetaSizer Nano ZS (Malvern Pananalytical, Westborough, MA, USA).

### 3.2.3. Ultramicroelectrode Fabrication

Pt UMEs were fabricated as described in previous literature.<sup>47</sup> A glass capillary was sonicated for 10 minutes in each water, ethanol, and isopropyl alcohol (IPA), then oven dried at 115°C for 30 minutes. While the capillary was drying, both ends of a length of insulated copper wire was cleaned by dipping it in IPA. After the capillary was dry, the copper wire was inserted into the capillary so the ends were sticking out. A  $\sim 1$  cm length of 5  $\mu\text{m}$  Pt microwire was cut and connected to the end of the copper wire on the thinner end of the capillary using a conductive silver epoxy (Epo-Teck H2OE, parts A and B mixed in equal amounts). The epoxy was allowed to cure in the 115°C oven overnight before the microwire was carefully pulled back into the capillary. The microwire end of the electrode was dipped in a mixture of a 15% w/w *m*-phenylenediamine and Epon Resin 828 heated to 50°C, then dried in the oven overnight. Finally, the open end of the electrode was sealed with Loctite EA 1C epoxy (2:1 A:B) and allowed to dry at room temperature overnight or until the Loctite epoxy was no longer tacky. Throughout the fabrication process, optical microscopy was used to monitor the quality of the electrode (straight microwire, no bubbles in resin, etc). The fabricated Pt UME was then gently sanded with wetted 600 grit sandpaper, then polished to a mirror finish with Buehler 0.05  $\mu\text{m}$  alumina powder in DI water on a Buehler micro-cloth pad. To quantify the radius of the fabricated Pt UME, a steady-state voltammogram was recorded in 50 mM  $\text{K}_4[\text{Fe}(\text{CN})_6]$  and 50 mM KCl. The radius ( $5.37 \pm 0.07$   $\mu\text{m}$ ;  $n = 5$ ) was calculated using Equation (26) from Section 1.3 using  $D_{[\text{Fe}(\text{CN})_6]^{4-}} = 6.98 \times 10^{-6} \text{ cm}^2 \text{ s}^{-1}$ .<sup>12</sup>

### 3.2.4. Cell Culturing and Bacteria Preparation

Luria Bertani (LB) broth was prepared as follows: 10 g of tryptone, 5 g of yeast extract, and 10 g of NaCl were quantitatively added to 1.0 L of water. The LB broth was then autoclaved for 45 minutes prior to use for cell culturing. A 100  $\mu$ L aliquot of 50% glycerol stock solution containing *Aeromicrobium erythreum* or *Bacillus subtilis* was added to 10 mL of LB broth and grown in a rotary shaker at 37°C for 24 hours (*B. subtilis*) or 48-72 hours (*A. erythreum*). Cell growth was monitored using optical density at 600 nm ( $OD_{600}$ ) measurements<sup>48</sup> and only bacteria in the stationary phase were used to perform experiments.

The concentration of the bacterial cells was calculated using  $OD_{600}$ . Cells were harvested by centrifuging 1 mL of the cell culture at 3,500 rpm for 5 minutes (*B. subtilis*) or 5,000 rpm for 8 minutes (*A. erythreum*).<sup>49</sup> The supernatant was removed and the pellet was resuspended in 1 mM phosphate buffer solution (PBS). The solution was centrifuged again before resuspending the cells in a solution of 100 mM  $K_4[Fe(CN)_6]$  and 1 mM KCl. All vials, tubes, and pipette tips were stored on a clean bench and cell cultures were stored in a sealed vial to avoid contamination.

## 3.3. Results and Discussion

### 3.3.1. Experimental Conditions for Blocking Signals by Bacterial Cells

Prior to bacterial detection experiments, an *i-t* curve was collected using 100 mM  $K_4[Fe(CN)_6]$  and 1 mM KCl to ensure signals were not arising from dust or other contaminants in the redox solution. As shown in the red trace in **Figure 13**, no signals or deviations from the steady-state current are observed in the absence of bacteria when a potential of +0.50V was applied to a Pt working disk ultramicroelectrode (radius  $5.37 \pm 0.07 \mu\text{m}$ ). While the bacteria were washed and resuspended in FCN to avoid dilution upon their addition to the electrochemical cell, the control test was repeated with an aliquot of un-inoculated LB broth added to the electrochemical cell, which also yielded no

deviations from the steady-state current. When *A. erythreum* or *B. subtilis* bacteria were added to the electrochemical cell, step-like decreases in current were observed, as in the black trace in **Figure 13**. All solutions were prepared fresh and sealed between uses, therefore, we assume that all current decreases arise from bacteria adsorbing to the electrode surface and decreasing the current flux. To analyze the step-like signals, the start point was defined as the coordinates at which the current deviated from the steady-state. The end of the step was defined as the coordinates as a few data points after the rise of the step.

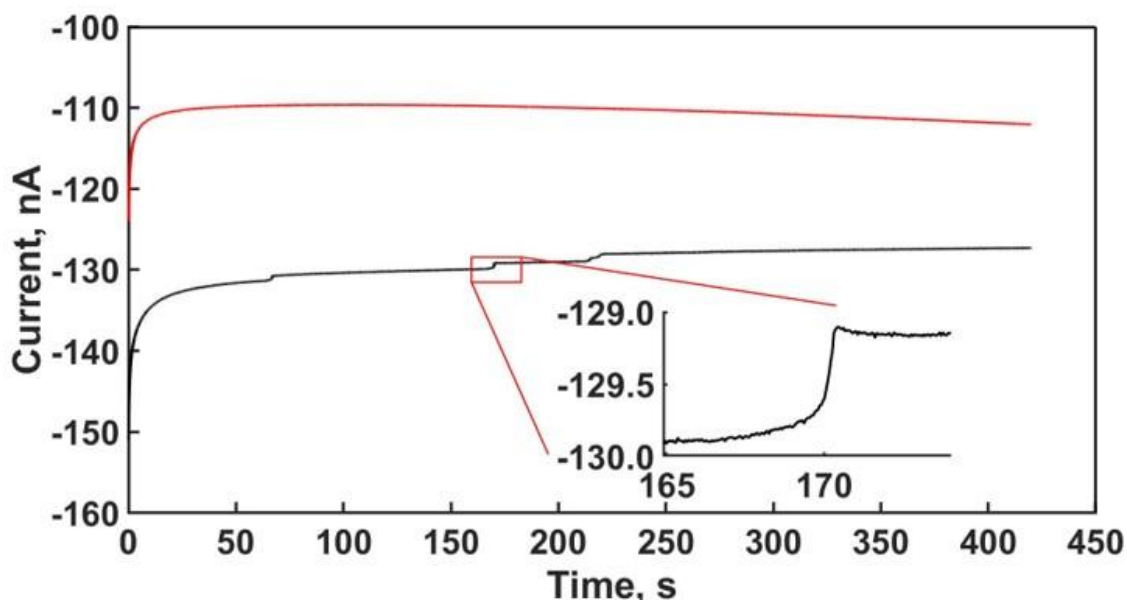


**Figure 13:** *i-t* curves with (black) and without (red) 10 fM *B. subtilis*. Inset reflects a single step enlarged to show detail. Pt UME; +0.50 V vs. 3M Ag/AgCl

To determine the maximum number of adsorption events at the electrode surface, the landing orientation of the bacteria must be known. Two likely landing positions are possible: end-on (vertical) or side-on (horizontal), as shown in **Figure 14A**. When a blocking collision occurs, the effective area of the electrode surface is changed according to

$$A_{net} = A_e - A_p \quad (40)$$

where  $A_{net}$  is the net area of the electrode after a spherical particle adsorbs,  $A_e$  is the area of the electrode, and  $A_p$  is the approximated area blocked by the bacteria. Substituting the equation for the area of a circle,  $A = \pi r^2$ , and solving for the net radius gives

$$r_{net} = \sqrt{r_e^2 - r_p^2} \quad (41)$$

where  $r_{net}$  is the net radius of the electrode after a spherical particle adsorbs,  $r_e$  is the radius of the electrode, and  $r_p$  is the radius of the adsorbed particle. Substituting  $r_{net}$  into the steady-state equation gives

$$i_{ss,p} = 4nFD_{[Fe(CN)_6]^{4-}}C_{[Fe(CN)_6]^{4-}}^* \sqrt{r_e^2 - r_p^2} \quad (42)$$

where  $n$  is the number of transferred electrons for the oxidation of potassium ferrocyanide,  $F$  is Faraday's constant (96485.34 C/mol),  $D_{[Fe(CN)_6]^{4-}}$  is the diffusion coefficient of potassium ferrocyanide ( $6.98 \times 10^{-6} \text{ cm}^2 \text{ s}^{-1}$ ),  $C_{[Fe(CN)_6]^{4-}}^*$  is the bulk concentration of potassium ferrocyanide (100 mM), and  $i_{ss,p}$  is the approximate steady-state current after the effective area of the electrode is reduced by the particle adsorbing to the electrode surface.

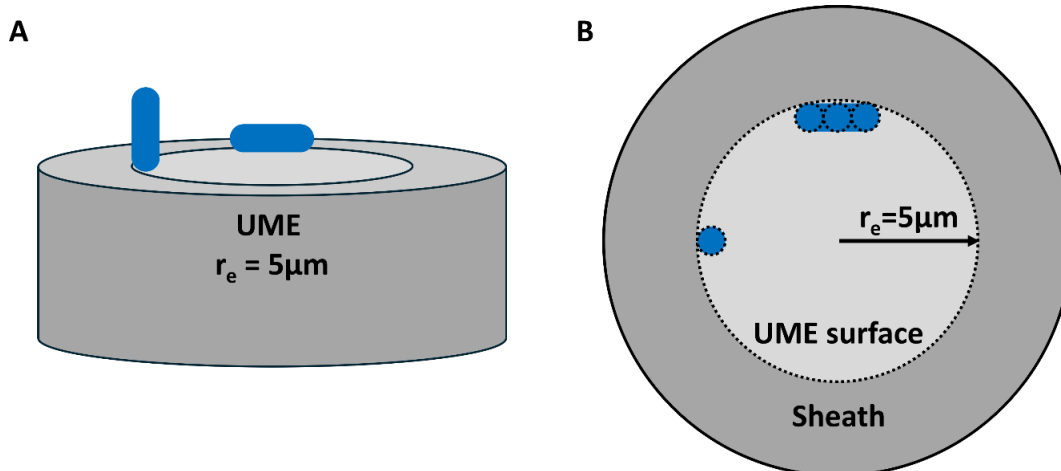


**Figure 14:** A) Proposed landing orientations of rod-shaped bacteria on the surface of an UME. B) Effect of bacteria on effective electrode surface area for two landing positions.

The size of the step can thus be approximated by equation (43).

$$i_{step} = i_{ss} - i_{ss,p} \quad (43)$$

For a rod-shaped bacterium, the horizontal landing orientation can be approximated as a series of circular particles (**Figure 14B**) and Equation (40) can be expanded as

$$A_{net} = A_e - \sum A_p \quad (44)$$

Substitution and rearrangement changes Equation (42) to

$$i_{ss,p} = 4nFD_{[Fe(CN)_6]^{4-}}C_{[Fe(CN)_6]^{4-}}^* \sqrt{r_e^2 - \sum r_p^2} \quad (45)$$

Substituting the size ranges of *B. subtilis* ( $1\mu\text{m} \times 2-6\mu\text{m}$ ) and *A. erythreum* ( $0.5\mu\text{m} \times 0.5-1.2\mu\text{m}$ ) into Equations (42),(43), and (45) yields the results in **Table 1**. For 391 observed *A. erythreum* steps, the average experimental current magnitude was  $0.12\text{ nA} \pm 0.06\text{ nA}$ , indicating that *A.*

*erythreum* typically adsorbs to the electrode vertically. For 103 observed *B. subtilis* steps, the average experimental current magnitude was  $0.4 \text{ nA} \pm 0.2 \text{ nA}$ , indicating that *B. subtilis* also typically adsorbs to the electrode vertically.

**Table 1:** Calculated step sizes for *A. erythreum* and *B. subtilis* at vertical and horizontal landing positions blocking the flux of potassium ferrocyanide (100 mM)

<i>A. erythreum</i>		
Vertical $i_{step}$ , nA	Minimum Horizontal $i_{step}$ , nA	Maximum Horizontal $i_{step}$ , nA
0.15	0.15	0.88
<i>B. subtilis</i>		
Vertical $i_{step}$ , nA	Minimum Horizontal $i_{step}$ , nA	Maximum Horizontal $i_{step}$ , nA
0.61	2.4	24.35

With an understanding of how each bacteria likely adsorbs to the electrode surface, the maximum number of bacteria cells that can adsorb to the electrode can be calculated. Using the surface area of the electrode and the blocked area of each bacterial cell,

$$Max. adsorption \# = \frac{A_e}{A_p} \quad (46)$$

Giving a maximum adsorption number of 400 cells for *A. erythreum* and 100 cells for *B. subtilis* on the surface of a  $5 \mu\text{m}$  radius electrode. However, insulating particles have been shown to adsorb more frequently to the electrode edge, due to the greater current density at the edge of UMEs. If bacteria are assumed to *only* land at the edge of the electrode, the area of the electrode

in a ring of width  $d_p$  (bacteria diameter) around the edge of the electrode will provide the maximum number of bacteria adsorptions. For *A. erythreum*, there are a total of 76 outer-edge adsorptions possible, and for *B. subtilis* there are a total of 36 outer-edge adsorptions possible. Overall, a minimum of five adsorption events is desired per  $i-t$  curve, which is readily achievable at the 5  $\mu\text{m}$  radius Pt disk UME we have chosen for these experiments.

### 3.3.2. Diffusion Coefficients of Bacterial Cells

In addition to predicting the possible surface coverage of an electrode, the predicted collisional frequency for bacteria moving solely by diffusion was also calculated. The advantage to doing this is twofold: first, we will gain an understanding of the minimum concentration required to see a certain number of steps within a given experimental time. Secondly, we can determine if we can compare the experimental and theoretical data to see if *B. subtilis* are moving to the electrode under their own power, by utilizing their flagella.<sup>50,51</sup> The frequency equation for a particle moving by diffusion is

$$f_{D_t} = 4D_t C_p r_e N_A \quad (47)$$

where  $f_{D_t}$  is the diffusional frequency,  $D_t$  is the translational diffusion coefficient,  $C_p$  is the concentration of the particle,  $r_e$  is the radius of the UME, and  $N_A$  is Avogadro's number. Generally, the diffusion coefficient for a spherical particle is calculated by

$$D_t = \frac{k_B T}{6\pi\eta r_p} \quad (48)$$

where  $k_B$  is Boltzmann's constant,  $T$  is the temperature,  $\eta$  is the viscosity, and  $r_p$  is the radius of the particle. However, only the smallest of the *A. erythreum* cells are spherical ( $D_t = 9.9 \times 10^{-9} \text{ cm}^2/\text{s}$ ). Following the model developed by Tirado and de la Torre<sup>52,53</sup>

$$D_t = \frac{k_B T}{3\pi\eta a} \left( \ln\left(\frac{a}{b}\right) + v \right) \quad (49)$$

where  $a$  is the cell length and  $b$  is the cell diameter. The last term,  $v$ , is a polynomial accounting for the shape of the bacilli, as follows

$$v = 0.312 + 0.565 \left(\frac{b}{a}\right) - 0.1 \left(\frac{b^2}{a^2}\right) \quad (50)$$

Equation (49) can thus be used to calculate the diffusion coefficients of rod-shaped *A. erythreum* and *B. subtilis*, and Equation (47) can be used to calculate the frequency. The diffusion coefficients and theoretical and experimental frequencies are given in **Table 2**, which shows that the experimental frequency is significantly higher than the theoretical frequency. This discrepancy indicates that even under diffusion-controlled conditions, bacteria are being drawn to the electrode surface. Movement by swimming or swarming is not possible in the case of the *A. erythreum*, as it is not a flagellated bacteria.

**Table 2:** Theoretical and experimental frequencies for *A. erythreum* and *B. subtilis* in diffusion-controlled blocking experiments. Diffusion coefficients are given for the smallest and largest possible sizes for *A. erythreum* (small: 0.5  $\mu\text{m}$  x 0.5  $\mu\text{m}$ ; large: 0.5  $\mu\text{m}$  x 1.2  $\mu\text{m}$ ) and *B. subtilis* (small: 1  $\mu\text{m}$  x 2  $\mu\text{m}$ ; large: 1  $\mu\text{m}$  x 6  $\mu\text{m}$ ). The theoretical frequency is given as a range for 50 fM of bacteria.

	Small $D_t, \text{cm}^2\text{s}^{-1}$	Large $D_t, \text{cm}^2\text{s}^{-1}$	$f_{\text{theoretical}}, \mu\text{Hz}$	$f_{\text{experimental}}, \mu\text{Hz}$
<i>A. erythreum</i>	$9.9 \times 10^{-9}$	$7.7 \times 10^{-9}$	377 – 597	2000
<i>B. subtilis</i>	$3.1 \times 10^{-9}$	$1.8 \times 10^{-9}$	109 – 189	36000

To determine if the discrepancies seen in **Table 2** are due to migration of the bacteria, the theoretical adsorption frequency due to migration was also calculated. At low concentrations of supporting electrolyte, the electric field grows, causing movement of charged particles toward the electrode surface when the electrode is biased at a potential that will electrostatically attract the charged particle. Equation (51) was used to calculate the migrational adsorption frequency,  $f_{mig}$ <sup>54</sup>

$$f_{mig} = \frac{i_{ss} C_p \mu_p}{e} \sum \frac{1}{c_i \mu_i} \quad (51)$$

where  $i_{ss}$  is the steady state current,  $C_p$  is the particle concentration,  $\mu_p$  is the particle's mobility, measured experimentally,  $e$  is the elementary charge,  $c_i$  is the concentration of ion  $i$ , and  $\mu_i$  is the mobility of ion  $i$ . For an experiment conducted in 100 mM potassium ferrocyanide with 1 mM KCl, the theoretical adsorption frequency for *A. erythreum* is 11 – 20 Hz. For *B. subtilis*, the theoretical adsorption frequency is 27 – 34 Hz. Experimentally, a much lower frequency is observed (0.007 Hz and 0.06 Hz for *A. erythreum* and *B. subtilis*, respectively), indicating that the bacteria are not moving to the electrode surface purely by migration. Due to the high concentration of the charged redox species ( $K_4[Fe(CN)_6]$ ), it is possible that the double layer is compacted more than predicted.

### 3.3.3. Effect of $\gamma$ on Collisional Frequency

To fully understand the relationship between the supporting electrolyte concentration, redox species concentration, and bacterial adsorption frequency, we employed the use of the value  $\gamma$ ,

$$\gamma = \frac{[Supporting\ Electrolyte]}{[Redox]} \quad (52)$$

Generally, for  $\gamma \leq 1$ , particles in solution move primarily by migration, while for  $\gamma > 1$ , diffusion dominates. Cyclic voltammograms and chronoamperometric  $i-t$  curves for a series of  $\gamma$  values were conducted, using the  $\gamma$  values given in **Table 3**, which also shows the experimentally observed frequencies across all parameters for *A. erythreum* and *B. subtilis*.

**Table 3:** Experimental frequencies of adsorption collisions for *A. erythreum* and *B. subtilis* at different values of  $\gamma$  encompassing diffusion-controlled mass transport, migration-controlled mass transport, and mixed mass transport.

$\gamma$	KCl, mM	K <sub>4</sub> [Fe(CN) <sub>6</sub> ], mM	$f_{experimental, Hz}$ <i>A. erythreum</i>	$f_{experimental, Hz}$ <i>B. subtilis</i>
0.01	0.5	50	0.004±0.005	0.08±0.03
0.01	1	100	0.007±0.005	0.06±0.02
0.1	1	10	0.005±0.003	0.04±0.01
0.1	5	50	0.006±0.004	0.07±0.01
0.1	10	100	0.004±0.002	0.06±0.02
1	50	50	0.009±0.006	0.06±0.01
1	100	100	0.002±0.005	0.036±0.005
10	100	10	0.0022±0.0008	0.007±0.004
50	500	10	0	0

**Figure 15-Figure 19** show the effect of  $\gamma$  on the cyclic voltammograms. For constant values of potassium ferrocyanide, the steady-state current does not change, although the CV becomes slightly less sigmoidal with decreasing supporting electrolyte concentration. CVs were normalized to compare equal  $\gamma$  with different redox species and supporting electrolyte concentration, which shows the greatest change in shape as the flux of the redox species is controlled by migration.

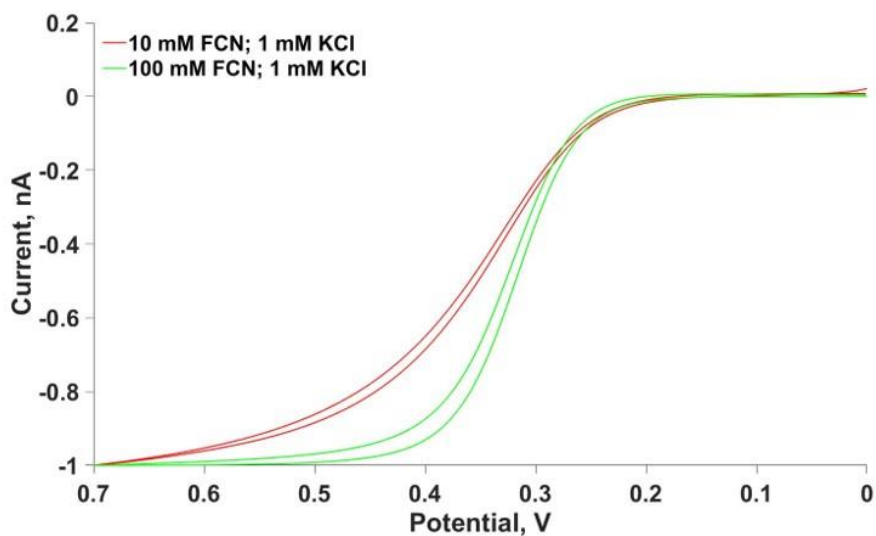


**Figure 15:** Normalized CVs for potassium ferrocyanide solutions containing 1 mM KCl (red,  $\gamma = 0.1$  ; green,  $\gamma = 0.01$ ). Scan rate: 10 mV/s. Pt working ultramicroelectrode (10  $\mu\text{m}$  diameter) vs 3 M Ag/AgCl

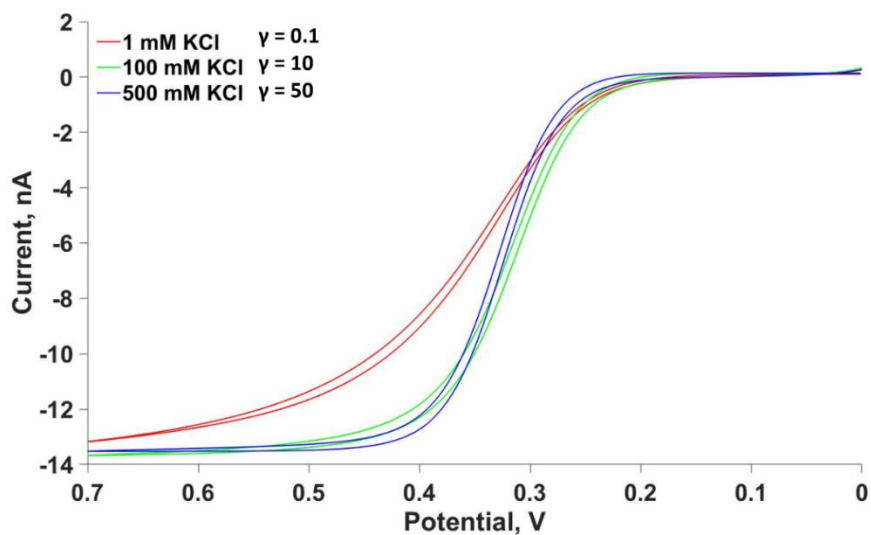


**Figure 16:** Cyclic voltammograms of different  $\gamma$  values (red,  $\gamma = 0.1$  ; green,  $\gamma = 10$ ; and blue,  $\gamma = 50$ ) with a constant potassium ferrocyanide concentration (10mM) vs Ag/AgCl. Scan rate: 10 mV/s. Pt working ultramicroelectrode (10 μm diameter) vs 3 M Ag/AgCl

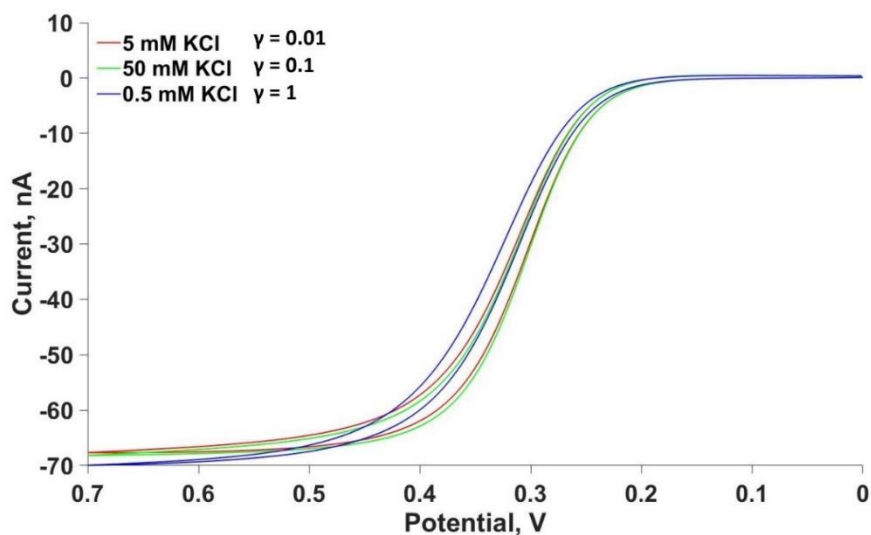


**Figure 17:** Cyclic voltammograms of different  $\gamma$  values (red,  $\gamma = 0.1$  ; green,  $\gamma = 1$ ; and blue,  $\gamma = 10$ ) with a constant potassium ferrocyanide concentration (50 mM). Scan rate: 10 mV/s. Pt working ultramicroelectrode (10 μm diameter) vs 3 M Ag/AgCl

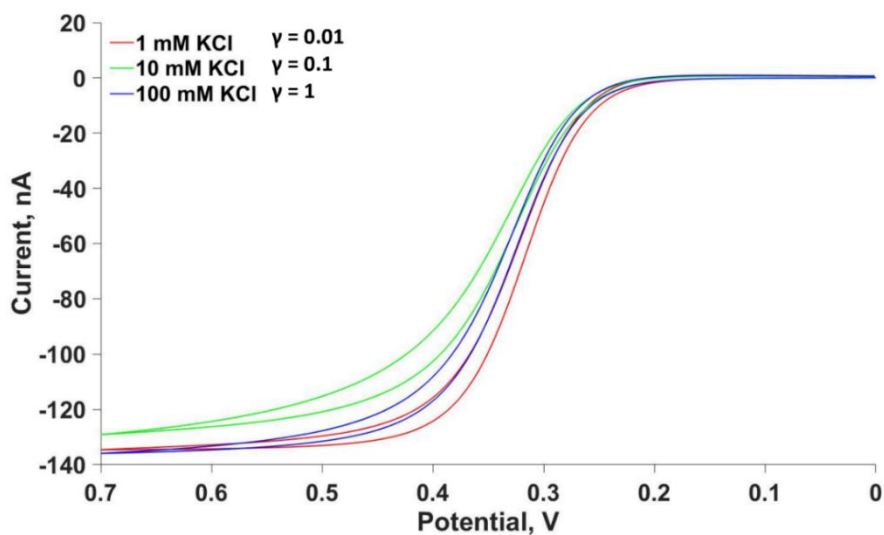


**Figure 18:** Cyclic voltammograms of different  $\gamma$  values (red,  $\gamma = 0.01$  ; green,  $\gamma = 0.1$ ; and blue,  $\gamma = 1$ ) with a constant potassium ferrocyanide concentration (100 mM). Scan rate: 10 mV/s. Pt working ultramicroelectrode (10  $\mu\text{m}$  diameter) vs 3 M Ag/AgCl

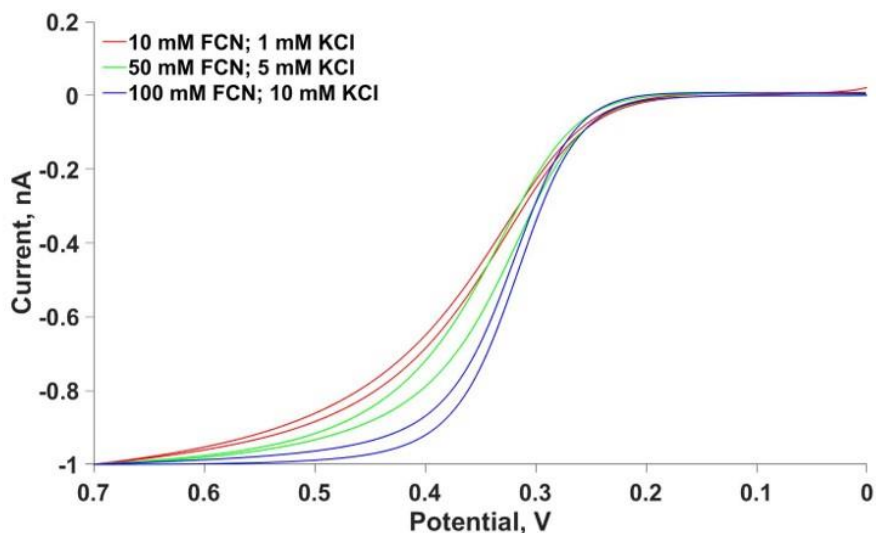


**Figure 19:** Normalized cyclic voltammograms for  $\gamma = 0.1$ . With decreasing potassium ferrocyanide concentration, the voltammograms become less sigmoidal. Scan rate: 10 mV/s. Pt working ultramicroelectrode (10  $\mu\text{m}$  diameter) vs 3M Ag/AgCl

### 3.4. Conclusions

In this work, step-like signals arising from the adsorption of two types of bacteria (*A. erythreum* and *B. subtilis*) were observed in chronoamperometric  $i-t$  curves. Prior to performing experiments,

the diffusion coefficient equation was adapted to rod-like bacteria following work done by Tirado and de la Torre. The resultant diffusion coefficient was used to predict the frequency of bacteria-electrode interactions under diffusion-controlled and migration-controlled conditions. We found that neither bacterium impacts the electrode in agreement with the theoretical frequency, either by diffusion or by migration. Potential causes, including the electrostatic attraction of the bacteria and the compaction of the double layer by the high concentration of the charged redox species were discussed. To fully quantify the relationship between the supporting electrolyte concentration, redox species concentration, and bacteria adsorption frequency, the parameter  $\gamma$  was used. Surprisingly, we found that the adsorption frequency was rather constant over multiple concentrations and ratios of KCl and  $K_4[(Fe(CN)_6)]$ . Future work should focus on quantifying the mode of mass transport influencing bacterial movement to the electrode surface, and the contribution of the bacteria's motility, if any.

# Chapter 4

## Bacterial Identification in Mixed Samples

Herein we propose that the step-like signals observed in blocking electrochemistry experiments can be analyzed by Savitzky-Golay filtering and that bacteria of different sizes can be discriminated by their size in mixed samples. First,  $i-t$  traces containing step-like signals are filtered using a quadratic first-derivative Savitzky-Golay filter, which converts the steps to spikes that MatLab can easily analyze. Each peak is integrated over its baseline width, providing each step's duration ( $\Delta t$ ) and current magnitude ( $\Delta i$ ). Bidimensional plots of  $\Delta t$  vs  $\Delta i$  are generated for *A. erythreum* and *B. subtilis* and compared to similar plots for mixed samples. Our results indicate the potential for the discrimination of bacteria in mixed samples

### 4.1. Introduction

The steps observed in chronoamperometric blocking experiments reflect the interaction of a single insulating particle adsorbing to the electrode surface. Since the ground-breaking work by Quinn et al, many types of particles have been examined by blocking electrochemistry.<sup>23,37,55-57</sup> As antibiotic resistant bacterial infections become more prevalent in the world, developing a fast and cost-effective method to quickly identify bacteria is of critical importance. In the past two decades, single-entity electrochemistry, and specifically blocking electrochemistry, has been investigated as a possible solution. Efforts have been frustrated by the inhomogeneous current density at the edge of ultramicroelectrodes (UMEs) causing uniform particles to create signals of varying signals.<sup>31,35</sup> Recent work has shown that bacilli perturb the flux of redox species to the electrode surface before they adsorb, and larger bacteria perturb the flux at a greater distance.<sup>47</sup> We build on this work to correlate the step magnitude and duration to the size of bacilli, creating bidimensional population density plots similar to those used in flow cytometry.

Typically, steps in chronoamperograms are analyzed by recording the point immediately before and after the rise of the step.<sup>14,23,35,47</sup> As a result, signal from bacteria perturbing the electric field before adsorbing to the electrode surface may be ignored. Accounting for the full duration that the bacterium interacts with the electrode may provide information about the size of the bacterial cell. However, detecting a change in slope on a baseline that is already sloping can be difficult. For this reason, and to facilitate a faster analysis of stepped  $i$ - $t$  curves, we apply a first-derivative Savitzky-Golay filter in MatLab, which transforms the step-like signals on a sloping steady-state baseline to spikes on a flat baseline.<sup>58</sup> Each spike is integrated over  $\Delta t = t_{end} - t_{start}$ , where  $t_{start}$  is taken as the point at which the signal fully deviates from the baseline and  $t_{end}$  as the point at which the signal returns to the baseline. With a  $\Delta t$  that is more reflective of the size of the bacterial cell, we plot  $\Delta i$  vs  $\Delta t$  to observe the population density of the size of the bacteria by proxy.

## 4.2. Experimental

### 4.2.1. Chemical Reagents

All reagents were used as received without further purification unless otherwise specified. Potassium hexacyanoferrate(II) trihydrate ( $K_4[Fe(CN)_6]$ , 98.5%), sodium chloride, sodium phosphate dibasic, and potassium phosphate monobasic were obtained from Sigma-Aldrich (St. Louis, MO, USA). Potassium chloride (KCl) was purchased from Thermo Fisher Scientific (Hampton, NH, USA). All aqueous solutions were prepared using Millipore water ( $\geq 18.2$  M $\Omega$ ·cm) unless otherwise specified.

### 4.2.2. Instrumentation

All electrochemical experiments were performed using a three-electrode setup in a single compartment electrochemical cell housed in a Faraday connected to a CHI 660C potentiostat (CHI Instruments, Austin, TX, USA). The three electrodes were a 3 M Ag/AgCl reference electrode, Pt

wire counter electrode, and a Pt working ultramicroelectrode ( $5.37 \mu\text{m} \pm 0.07 \mu\text{m}$  radius) prepared as described in Section 3.2.3. Before and between experiments, the Pt UME was polished to a mirror finish with  $0.05 \mu\text{m}$  alumina powder (Buehler, Lake Bluff, IL, USA) slurry on a Buehler micro-cloth polishing pad. Scanning electron microscopy (SEM) was completed using a Hitachi SU-70 FE-SEM operating at 5 kV. Critical drying of samples in preparation for SEM was achieved using an Autosamdri-931 (Rockville, MD, USA). Zeta potential experiments were performed using a ZetaSizer Nano ZS (Malvern Pananalytical, Westborough, MA, USA).

### **4.2.3. Cell Culturing and Bacteria Preparation**

Cell culturing was conducted as described in Section 3.2.4. Briefly, Luria Bertani (LB) broth was prepared, then autoclaved for 45 minutes prior to use for cell culturing. One colony-forming unit (CFU) was removed from an agar plate containing *Aeromicrobium erythreum* or *Bacillus subtilis* and added to 10 mL of LB broth and grown in a rotary shaker at  $37^\circ\text{C}$  for 24 hours (*B. subtilis*) or 48-72 hours (*A. erythreum*). Cell growth was monitored using optical density at 600 nm ( $\text{OD}_{600}$ ) measurements and only bacteria in the stationary phase were used to perform experiments.

The concentration of the bacterial cells was calculated using  $\text{OD}_{600}$ . Cells were harvested by centrifuging 1 mL of the cell culture at 3,500 rpm for 5 minutes (*B. subtilis*) or 5,000 rpm for 8 minutes (*A. erythreum*). The supernatant was removed, and the pellet was resuspended in 1 mM phosphate buffer solution (PBS). The solution was centrifuged again before resuspending the cells in a solution of 100 mM  $\text{K}_4[\text{Fe}(\text{CN})_6]$  and 1 mM KCl. All vials, tubes, and pipette tips were stored on a clean bench and cell cultures were stored in a sealed vial to avoid contamination.

### **4.2.4. Data Collection and Analysis**

Electrochemical experiments were recorded using CH Instrument's CHI660 v18.01 software. Data analysis was performed using a homemade MatLab (R2019a) script to calculate step magnitude and duration (blocking current and time change; Appendix A: MatLab Script for

Savitzky-Golay Filtering). Steps were manually counted and analyzed to confirm the accuracy of the MatLab script.

## 4.3. Results and Discussion

### 4.3.1. Convolution of Bacterial *i-t* Curve by Application of First Derivative Savitzky-Golay Filter

Savitzky-Golay filtering is a popular least-squares procedure that averages  $2m + 1$  successive data points in a data set to smooth noise. Generally, the filter is written as

$$a_{nsm} = s! b_{nsm} = \sum_{i=-m}^{i=m} \frac{C_{ism} y_i}{\Delta x^s N_{sm}} \quad (53)$$

where  $a_{nsm}$  is the  $s^{th}$  derivative of the window  $2m + 1$ , which encompasses  $y_{i=-m}$  to  $y_{i=m}$ , centered around point  $i = 0$ . This general formula solves the best mean square fit for a polynomial of degree  $n$  (less than  $2m + 1$ ), which is solved by

$$f_i = \sum_{k=0}^{k=n} b_{nk} i^k = b_{n0} + b_{n1} i + b_{n2} i^2 + \dots + b_{nn} i^n \quad (54)$$

The derivative of the polynomial can be expressed as

$$\frac{d^n f_i}{d i^n} = n! b_{nn} \quad (55)$$

As a note, the center of the moving window,  $i = 0$ , and thus the value of the  $s^{th}$  derivative at  $i = 0$  is written as

$$\left(\frac{d^s f_i}{dt^s}\right)_{i=0} = s! b_{ns} = a_{ns} \quad (56)$$

The method of least squares requires that the sum of the squares of the difference between the observed and calculated values ( $y_i$  and  $f_i$ , respectively) be a minimum over the interval  $-m - m$ , such that

$$0 = \frac{\delta}{\delta b_{nk}} \left[ \sum_{i=-m}^{i=m} (f_i - y_i)^2 \right] \quad (57)$$

Minimizing with respect to  $b_{ni}$  leads to

$$0 = \frac{\delta}{\delta b_{ni}} \left[ \sum_{i=-m}^{i=m} (b_{n0} + b_{n1}i + b_{n2}i^2 + \dots + b_{nn}i^n - y_i)^2 \right] \quad (58)$$

Simplifying leads to

$$0 = 2 \sum_{i=-m}^{i=m} (b_{n0} + b_{n1}i + b_{n2}i^2 + \dots + b_{nn}i^n - y_i)i \quad (59)$$

If we repeat the above for a more generalized  $b_{nr}$ , where  $r$  represents the index of each equation, numbered 0 to  $n$ ,

$$0 = 2 \sum_{i=-m}^{i=m} \left[ \left( \sum_{k=0}^{k=n} b_{nk}i^k \right) - y_i \right] i^r \quad (60)$$

which can be rearranged to

$$\sum_{i=-m}^{i=m} i^{k+r} \sum_{k=0}^{k=n} b_{nk} = \sum_{i=-m}^{i=m} y_i i^r \quad (61)$$

Setting the first term equal to  $S_{r+k}$

$$S_{r+k} = \sum_{i=-m}^{i=m} i^{k+r} \quad (62)$$

and the right term equal to  $F_r$

$$F_r = \sum_{i=-m}^{i=m} y_i i^r \quad (63)$$

For odd values of  $r + k$ ,  $S_{r+k} = 0$ , which means if we solve for a first-derivative polynomial of  $n = 4 \dots$

Eq 1:

$$r=0 \quad S_{0+0}b_{40} + S_{0+1}b_{41} + S_{0+2}b_{42} + S_{0+3}b_{43} + S_{0+4}b_{44} = F_0$$

Simplifying leads to...

$$S_0b_{40} + S_1b_{41} + S_2b_{42} + S_3b_{43} + S_4b_{44} = F_0 = S_0b_{40} + 0 + S_2b_{42} + 0 + S_4b_{44}$$

Finally

$$F_0 = S_0b_{40} + S_2b_{42} + S_4b_{44}$$

Thus, for all values of  $F_r$ , grouped by odd and even functions

$$F_0 = S_0 b_{40} + S_2 b_{42} + S_4 b_{44}$$

$$F_2 = S_2 b_{40} + S_4 b_{42} + S_6 b_{44}$$

$$F_4 = S_4 b_{40} + S_6 b_{42} + S_8 b_{44}$$

$$F_1 = S_2 b_{41} + S_4 b_{43}$$

$$F_3 = S_4 b_{41} + S_6 b_{43}$$

Only the odd functions ( $F_1$  and  $F_3$ ) will be dealt with from this point forward. By substitution and rearrangement, a solution is found for  $b_{41}$

$$b_{41} = \frac{S_6 F_1 - S_4 F_3}{S_2 S_6 - S_4^2} \quad (64)$$

For  $m = 2$ ,  $S_2$ ,  $S_4$ , and  $S_6$  can be solved from Equation (62),

$$S_2 = (-2^2) + (-1^2) + (0^2) + (1^2) + (2^2) = 10$$

$$S_4 = (-2^4) + (-1^4) + (0^4) + (1^4) + (2^4) = 34$$

$$S_6 = (-2^6) + (-1^6) + (0^6) + (1^6) + (2^6) = 130$$

and  $F_1$  and  $F_3$  can be expanded from Equation (63),

$$F_1 = (-2_{y-2})^1 + (-1_{y-1})^1 + (0_{y0})^1 + (1_{y+1})^1 + (2_{y+2})^1$$

$$F_3 = (-2_{y-2})^3 + (-1_{y-1})^3 + (0_{y0})^3 + (1_{y+1})^3 + (2_{y+2})^3$$

which can be combined into Equation (64)

$$b_{41} = \frac{130F_1 - 34F_3}{144}$$

$$b_{41} = \frac{1_{y-2} - 8_{y-1} + 0_{y0} + 8_{y+1} - 1_{y+2}}{12}$$

Thus, for a first-derivative polynomial of  $n = 4$ , the coefficients of the moving window are 1,  $-8$ , 0, 8, and  $-1$ , with a normalization factor of  $N = 12$ , which are in agreement with Table IV in the initial publication.<sup>58</sup>

For this work, a first-derivative polynomial of  $n = 2$  was used to apply a moving window of size  $2m + 1$  to successive, adjacent data points in the data set  $\{t_j, i_j\}$ , where  $j = 1, 2, 3, \dots, n$  represents the index in the original data set by Equation (65):

$$I_j = \frac{\Delta i_j}{\Delta t_j} = \sum_{i=-m}^{i=m} \frac{C_i i_{j+i}}{N dt} \quad (65)$$

where  $I_j$  is the convoluted data point (nA/s),  $C_k$  is the  $k$  convolution coefficient,  $dt$  is the sampling interval, and  $N$  is the  $2m + 1$  -point normalization factor.  $C_k$  and  $N$  can be calculated as above or obtained from tables of Savitzky-Golay convolution coefficients and normalization factors. The resulting  $\{t_j, I_j\}$  derivative plots have spike-like features on a flat baseline in place of the step-like features on a sloping baseline, as shown in **Figure 20**. The size of the moving window, or the

number of successive, adjacent data points derived at once, directly affects the noise, intensity, and width of the signal observed in the derivative plot **Figure 21**. Thus, the size of the moving window was arbitrarily limited to less than 0.75 seconds following Equation 2:

$$n \geq \frac{0.75}{dt} \quad (66)$$

where  $n$  is the size of the moving window, rounded to the nearest odd integer.

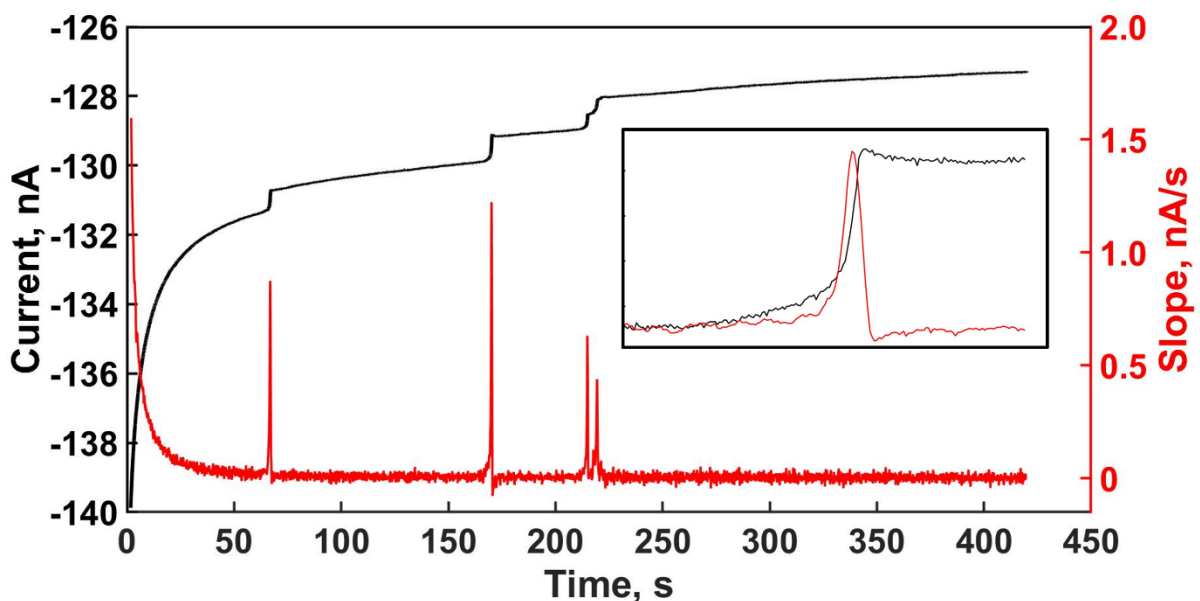


**Figure 20:** Chronoamperometric  $i$ - $t$  trace (black) of 50 fM *B. subtilis* in 100 mM  $K_4[Fe(CN)_6]$  and 1 mM KCl. Following application of an 11-point, quadratic first-derivative Savitzky-Golay filter (red), spikes that closely match the location of the steps appear in the convoluted trace. The inset shows a spike overlaid on a step to demonstrate the similarities between the signals.

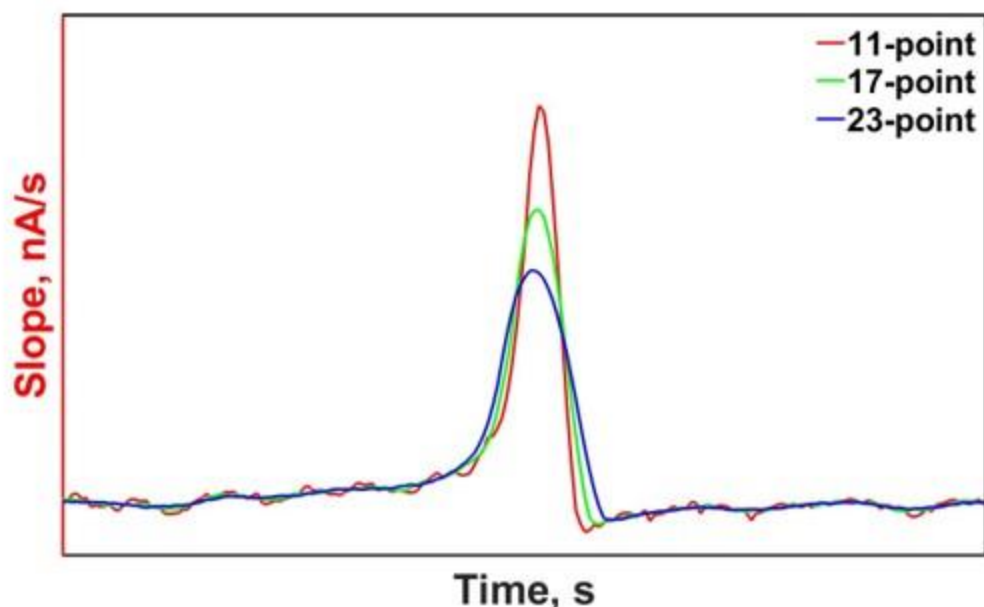


**Figure 21:** The effect of an increased window size. While noise is decreased with an increasing window size, the resolution and intensity of the signal is also decreased.

Following the application of the Savitzky-Golay filter, the spike-like signals were defined as arising from bacteria adsorbing to the electrode surface only if the local maxima of the peak was greater than three times the standard deviation of the baseline.<sup>59</sup> Due to the exponential decay curve at the beginning of each trace, the baseline is taken as a segment of the Savitzky-Golay plot containing no signal. The start and end points of the peaks were defined as the point that the signal deviated from the baseline and returned to the baseline, respectively. One notable exception was near-simultaneous adsorption events, producing two step-like signals. In these cases, the start of the first spike-like signal was defined as other spike-like signals, while the end was defined as the local minima between the signals. The same point was defined as the start of the second spike-like signal, with the end defined as other spike-like signals. The area under the curve of each peak between the start and end times,  $\Delta t$ , provided the magnitude of the blocked current,  $\Delta i$ . Ten  $i$ - $t$  curves were analyzed manually and compared to the values obtained from the filtered data. Table 2 shows a sampling of the total number of steps analyzed. Generally, there is

good agreement between both values, with an average deviation of 4 pA and 0.18 s between the manual and MatLab analysis, with MatLab generating the smaller values more frequently. The larger difference in step duration can likely be attributed to nuanced changes in the flat baseline of the SG plot being more noticeable than changes in the slope of an  $i-t$  curve.

**Table 4:** Comparison of step duration and current magnitudes obtained from manual analysis of each step listed to those obtained from the MatLab script.

$\Delta i$ , nA		$\Delta t$ , s	
Manual Analysis	MatLab Analysis	Manual Analysis	MatLab Analysis
0.423	0.403	2.142	1.637
0.221	0.211	1.468	1.518
0.138	0.142	2.099	1.872
0.327	0.312	1.174	0.845
0.078	0.101	0.923	1.014

### 4.3.2. Discrimination of *A. erythreum* and *B. subtilis* in Mixed Samples

An overlay of the Savitzky-Golay plots for *A. erythreum* and *B. subtilis* revealed an overall difference in the magnitude and frequency of the spike-like signals **Figure 22**. To determine the viability of using  $\Delta i$  and  $\Delta t$  as proxies for bacteria size, the two were plotted against each other. The resulting scatter plot revealed information about the population densities of the two bacteria relative to each other **Figure 23**. By taking the average and standard deviation ( $\sigma$ ) of  $\Delta i$  and  $\Delta t$ , a box encompassing  $\pm\sigma$  can be imposed, showing where 68% of all data values for each bacteria

species is located. Due to the non-homogenous flux of redox species at the surface of a disk UME and the size range of the bacterial cells (*A. erythreum*:  $0.5\mu\text{m} \times 0.5 - 1.2\mu\text{m}$ ; *B. subtilis*:  $1\mu\text{m} \times 2 - 6\mu\text{m}$ ), the range of  $\Delta i$  and  $\Delta t$  values is quite large. However, the more tightly clustered population density of *A. erythreum* and the less tightly clustered population density of *B. subtilis* indicate that the bidimensional plots provide a good proxy for bacteria size. To test this theory, 10 fM of *A. erythreum* was mixed with 10 fM of *B. subtilis* and the resulting steps were used to create a bidimensional plot with the boxes from the unmixed data (**Figure 24**). While the data in the mixed plots was skewed slightly to the left, the boxes generally encompass 60% of the data points, which is in good agreement with the unmixed plot.

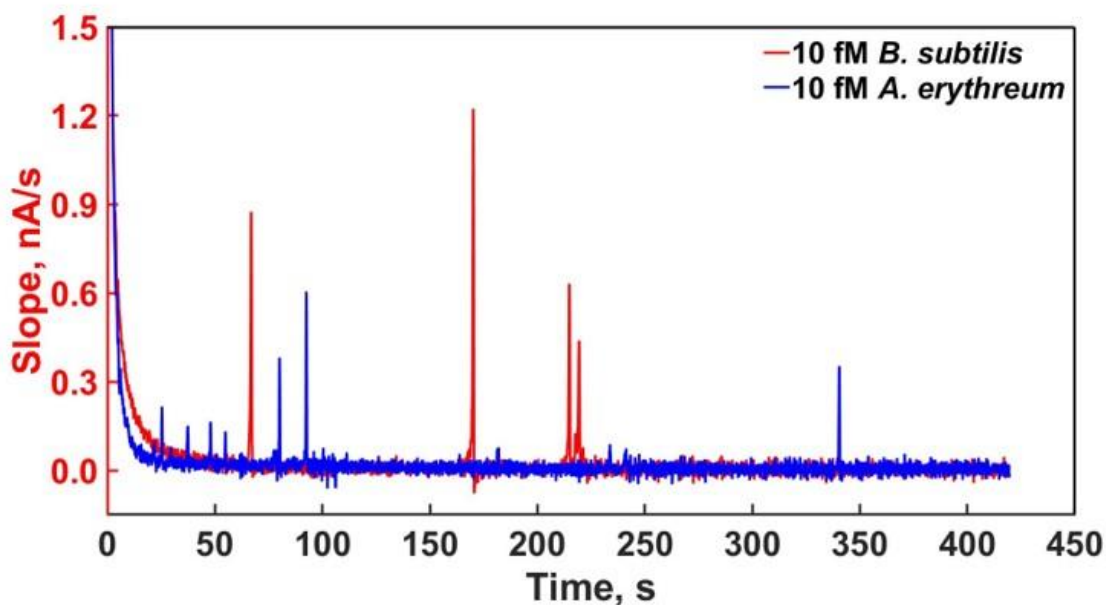


**Figure 22:** 11-pt 1<sup>st</sup> derivative Savitzky-Golay plots of *A. erythreum* and *B. subtilis*.

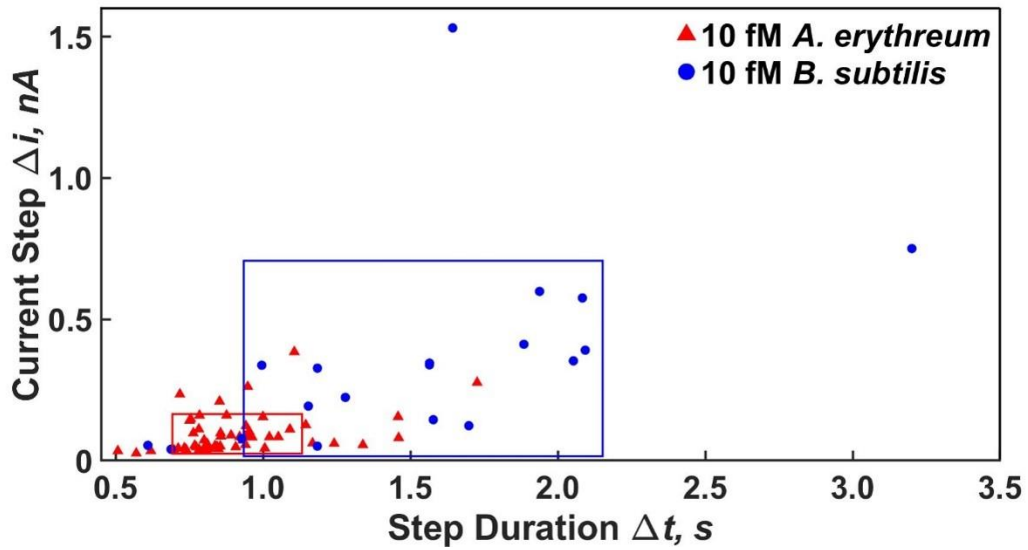


**Figure 23:** Bidimensional population density plot of *A. erythreum* and *B. subtilis* with boxes  $\pm 1\sigma$  in the x- and y-directions around the average.

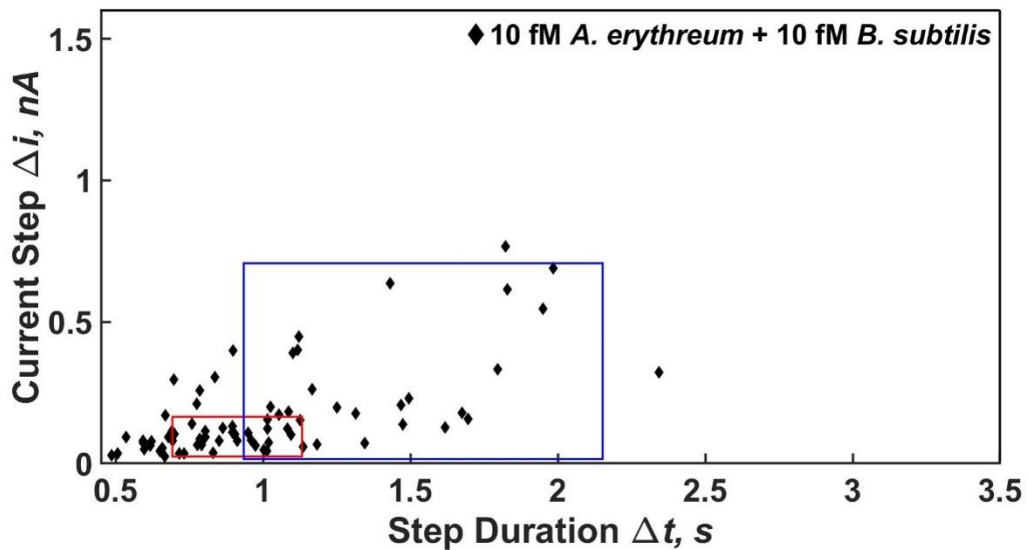


**Figure 24:** Bidimensional population density plot of mixed *A. erythreum* and *B. subtilis* with boxes  $\pm 1\sigma$  in the x- and y-directions around the average from **Figure 23**.

## 4.4. Conclusions

In this work we developed a method of analyzing  $i-t$  curves with step-like signals by applying a quadratic Savitzky-Golay filter to obtain spike-like signals in a flat baseline. Each spike was integrated over the duration of the spike, where the start and end times were defined as the time that the signal fully deviated from the baseline, and the time that the signal returned to the baseline. The results were in good agreement with those obtained from a manual analysis of the same  $i-t$  curve, though the  $\Delta t$  generally deviated more than  $\Delta i$ . The deviation is likely due to the spike starting within a flat baseline. We also proposed a method to discriminate bacteria by size in mixed samples, using bidimensional population density plots. Our results show that the larger bacteria, which perturb the flux of the redox species to the electrode surface at a greater distance than the smaller bacteria, have larger  $\Delta t$  and  $\Delta i$  values, which is reflected in the population density plots. In future, work in this area should focus on increasing the separation of the population densities, or introducing a monodisperse particle to act as a standard within the population density plots.

# Chapter 5

## Electrochemical Determination of Cell Viability

Here, single-entity electrochemistry is shown to be a viable tool to monitor the efficacy of antibiotics. Rapid and cost-effective methods to monitor the response of bacteria to antibiotics is an important topic in healthcare as deaths related to antibiotic-resistant bacteria continue to rise. Valinomycin is an ionophoric antibiotic that kills cells by selectively transporting potassium ions across the cell membrane. This work shows that *B. subtilis* cells exposed to an inhibitory concentration of valinomycin, with and without extracellular potassium ions, exhibit a slight decrease in the magnitude of their zeta potential after exposure. Additionally, the step-like signals typically observed in *i-t* curves transform to hump-like signals and exhibit a greater amount of noise post-adsorption. However, the transformed signals slowly return to their pre-exposure, step-like signals two hours post-exposure. The transformation in signal may arise from the increased zeta potential or inhibition of motility. The return to step-like signals likely arises from the reversal of inhibition.

### 5.1. Introduction

With the rapid rise of antibiotic-resistant bacteria, the need to develop rapid, cost-effective techniques to monitor the efficacy of antibiotics in real-time is extremely important. It was recently estimated that more than 700,000 people around the world die each year due to antibiotic-resistant infections,<sup>21,46</sup> a staggering number that is sure to continue to grow without new techniques and drugs to address the issue. Typically, the minimum inhibitory concentration (MIC), or the minimum concentration of an antibiotic required to prevent visible growth of a particular bacterial species.<sup>46,60</sup> However, at the MIC, there is generally an antibiotic-resistant subspecies that survives and proceeds to proliferate, developing antibiotic-resistance for all future colonies originating from it.

Single-entity electrochemistry offers detection of bacteria at the single cell level.<sup>14,23,33,40</sup> Previous work has shown blocking electrochemistry, used for insulating particles, like bacteria, has potential as a rapid and inexpensive technique in the fields of bacterial detection and identification. Herein, we propose to extend blocking electrochemistry to monitor the efficacy of antibiotics on bacteria post-exposure. Valinomycin, shown in **Figure 25**, is a dodecadepsipeptide antibiotic that catastrophically disrupts metabolic processes of cells by selectively transporting  $K^+$  out of the cell, disrupting the electrochemical gradient across the cell membrane.<sup>61,62</sup> At lower concentrations, valinomycin has been shown to decrease the proton-motive force across the cell membrane, thereby inhibiting motility of the bacteria.<sup>63</sup> At these lower concentrations, *B. subtilis* has also been shown to reverse the inhibitory effect of valinomycin over time.<sup>63</sup>

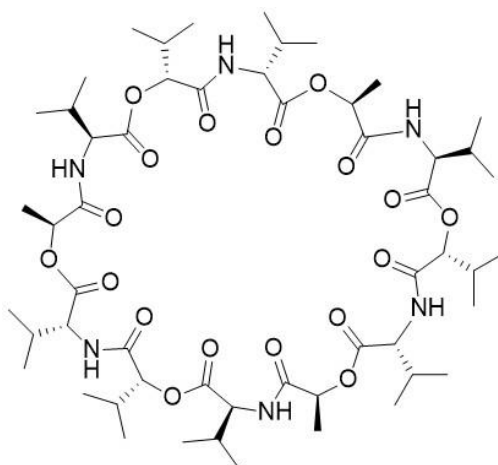


**Figure 25:** Structure of valinomycin, an antibiotic compound that inhibits cells by transporting potassium ions through the cell membrane

To monitor the efficacy of valinomycin on *B. subtilis*, which is highly affected by the antibiotic,<sup>64</sup> we first measured the effect of  $K^+$  and valinomycin on the zeta potential of the cells. Changes in zeta potential would directly affect the cell's mass transport in an electrochemical cell, to the effect that the step-like signals typically observed might change. If the magnitude of the bacteria's zeta

were decreased, we might expect to see a step with a greater temporal aspect, while if it were increased, we might expect to see a decrease in the temporal aspect of steps. Similarly, the effect of valinomycin on the structure of the cell may affect the observed signals. With this in mind, a low concentration of valinomycin is used for our initial experiments. If the cell is deformed post-valinomycin exposure, a larger electrode area may be blocked, resulting in larger average signals appearing in the *i-t* traces. Alternatively, if the cells are lysed, an overall decrease in the frequency of signals would likely be observed. As has been shown by previous work, the mechanism of action of the antibiotic, and thus how the cell dies, plays a significant role in the signals observed in the chronoamperogram. Herein, we report that valinomycin changes the zeta potential of *B. subtilis* cells and transforms the signals observed in *i-t* traces over time.

## 5.2. Experimental

### 5.2.1. Chemical Reagents

All reagents were used as received without further purification unless otherwise specified. Potassium hexacyanoferrate(II) trihydrate ( $K_4[Fe(CN)_6]$ , 98.5%), sodium chloride, sodium phosphate dibasic, and potassium phosphate monobasic were obtained from Sigma-Aldrich (St. Louis, MO, USA). Potassium chloride (KCl) was purchased from Thermo Fisher Scientific (Hampton, NH, USA). Valinomycin was donated. All aqueous solutions were prepared using Millipore water ( $\geq 18.2 \text{ M}\Omega\cdot\text{cm}$ ) unless otherwise specified.

### 5.2.2. Instrumentation

All electrochemical experiments were performed using a CHI 660C potentiostat (CHI Instruments, Austin, TX, USA) with a three-electrode setup in a single-compartment electrochemical cell housed in a Faraday cage. The electrode setup was comprised of a 3 M Ag/AgCl reference electrode, Pt wire counter electrode, and a Pt working ultramicroelectrode (UME) prepared as described in 3.2.3. Before and between experiments, the Pt UME was

gently polished with 0.05  $\mu\text{m}$  alumina powder (Buehler, Lake Bluff, IL, USA) slurry on a Buehler polishing pad. Zeta potential measurements were performed using a ZetaSizer Nano ZS (Malvern Pananalytical, Westborough, MA, USA).

### 5.2.3. Cell Culturing and Bacteria Preparation

Luria Bertani (LB) broth was prepared as follows: 10 g of tryptone, 5 g of yeast extract, and 10 g of NaCl were quantitatively added to 1.0 L of water. The LB broth was then autoclaved for 45 minutes prior to use for cell culturing. A 100  $\mu\text{L}$  aliquot of 50% glycerol stock solution containing *Aeromicrobium erythreum* or *Bacillus subtilis* was added to 10 mL of LB broth and grown in a rotary shaker at 37°C for 24 hours (*B. subtilis*) or 48-72 hours (*A. erythreum*). Cell growth was monitored using optical density at 600 nm ( $\text{OD}_{600}$ ) measurements and only bacteria in the stationary phase were used to perform experiments.<sup>48</sup>

The concentration of the bacterial cells was calculated using  $\text{OD}_{600}$ . Cells were harvested by centrifuging 1 mL of the cell culture at 3,500 rpm for 5 minutes (*B. subtilis*) or 5,000 rpm for 8 minutes (*A. erythreum*).<sup>49</sup> The supernatant was removed and the pellet was resuspended in 1 mM phosphate buffer solution (PBS). The solution was centrifuged again before resuspending the cells in a solution of 100 mM  $\text{K}_4[\text{Fe}(\text{CN})_6]$  and 1 mM KCl with or without 1  $\mu\text{M}$  valinomycin. All vials, tubes, and pipette tips were stored on a clean bench and cell cultures were stored in a sealed vial to avoid contamination.

### 5.2.4. Data Collection and Analysis

Electrochemical experiments were recorded using CH Instrument's CHI660C v18.01 software.

## 5.3. Results and Discussion

### 5.3.1. Effect of Valinomycin on Zeta Potential and Observed Chronoamperometric Signal of *B. subtilis*

To quantify the effect of low concentrations of KCl and valinomycin on the zeta potential of *B. subtilis* over time, we performed a series of zeta potential measurements. In the presence of no KCl and no valinomycin, the zeta potential was  $-41 \pm 6$  mV, which remained relatively constant over two hours. In the presence of only KCl, the *B. subtilis* zeta potential was  $-44 \pm 8$  mV, which also remained relatively constant over two hours. In the presence of valinomycin, the bacteria's zeta potential was  $-35 \pm 6$  mV, which did not change over time. Finally, in the presence of both KCl and valinomycin, the *B. subtilis* zeta potential was  $-35 \pm 7$  mV, which did not change over time. These results are detailed in **Table 5**. There appears to be some effect on the average zeta potential, though the large standard deviations do not lend credence to it being a statistically significant difference. In addition to the zeta potential measurements, the bacteria in the presence of KCl and valinomycin was monitored by optical microscopy. Over time, the cells appear to decrease in concentration and fade, perhaps indicating lysis of some cells.

**Table 5:** Effect of KCl and valinomycin on the zeta potential of *B. subtilis* from immediately after exposure ( $t = 0$ ) to three hours ( $t = 3$ ) after exposure

KCl	Valinomycin	Zeta Potential, mV		
		$t = 0 \text{ hr}$	$t = 1 \text{ hr}$	$t = 2 \text{ hr}$
–	–	$-41 \pm 6$	$-41 \pm 6$	$-44 \pm 6$
+	–	$-44 \pm 8$	$-45 \pm 7$	$-40 \pm 7$
–	+	$-35 \pm 6$	$-36 \pm 6$	$-36 \pm 6$
+	+	$-35 \pm 7$	$-35 \pm 6$	$-36 \pm 7$

With the understanding of the physical and electrochemical effects of valinomycin on *B. subtilis*, we further analyzed the effects of the antibiotic on the signals observed in  $i$ - $t$  curves. Interestingly, we found that the chronoamperograms no longer contained only steps. **Figure 26** shows representative signals observed in the  $i$ - $t$  curve immediately after exposure ( $t = 0$  hr). While the general step shape is still present, it is distorted by long  $\Delta t$ 's or the appearance of extra noise immediately following the step. The post-signal noise could be due to the movement of the adsorbed cell as it settles into a lower energy position on the electrode surface. Notably, three of the four signals observed in **Figure 26(A-C)** appear to return to the steady state as it would have been if the bacterium had not adsorbed. This could indicate detachment of the cells from the electrode surface, though correlated microscopy studies would need to be completed to confirm this. Chronoamperometric  $i$ - $t$  curves were also recorded at time  $t = 1$  hr and  $t = 2$  hr. As can be seen in **Figure 26-Figure 28**, the signals slowly return to solely step-like signals observed in the  $i$ - $t$  curve, as in **Figure 28A**. The transformation of the signals from step-like to hump-like may be

due to the changed zeta potential of the *B. subtilis* cells. However, it could also arise from the inhibition of the cells' motility by valinomycin. The return to step-like signals in the second hour is likely due to the bacteria's reversal of the inhibitory effect of the valinomycin. The continued observation of post-signal noise may be attributed to long-term effects of the antibiotic on the bacteria.

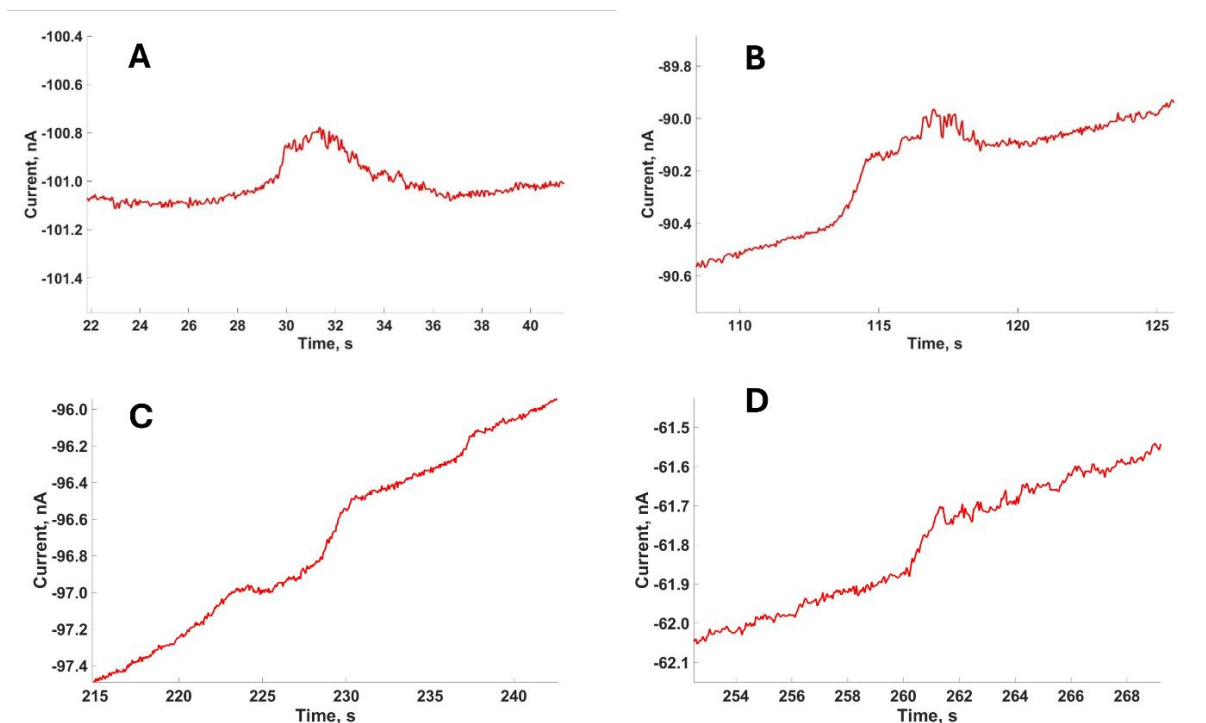


**Figure 26:** Four steps observed in *i-t* curves recorded of *B. subtilis* immediately after ( $t = 0$ ) exposure to  $1 \mu\text{M}$  valinomycin. While a generally “step-like” shape is observed in A-D, a subsequent increase in signal is observed in A and B. In A, B, and D, an increase in noise is observed immediately following the step, which may be attributed to movement of the adsorbed cell.

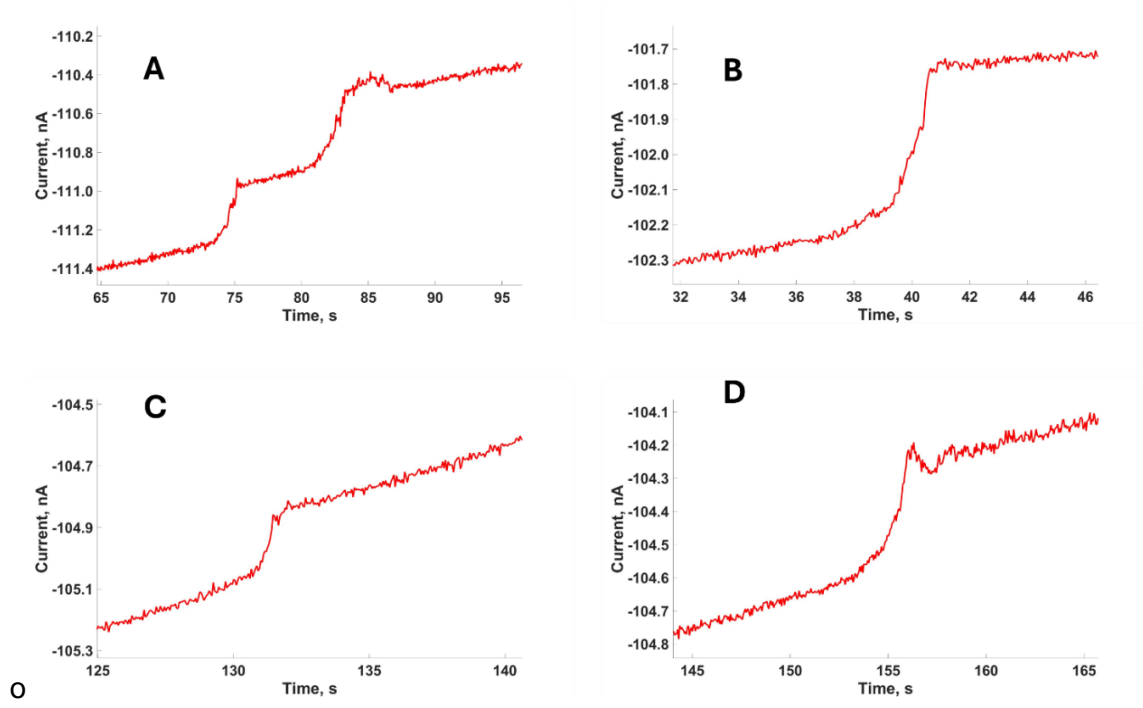


**Figure 27:** Four steps observed in  $i-t$  curves recorded of *B. subtilis* 1 hour after ( $t = 1 \text{ hr}$ ) exposure to  $1 \mu\text{M}$  valinomycin. While step-like shapes are observed in A-D, a subsequent increase in signal is observed in the second signal in A. In A and D, an increase in signal variation is observed immediately following the step, which may be attributed to movement of the adsorbed cell

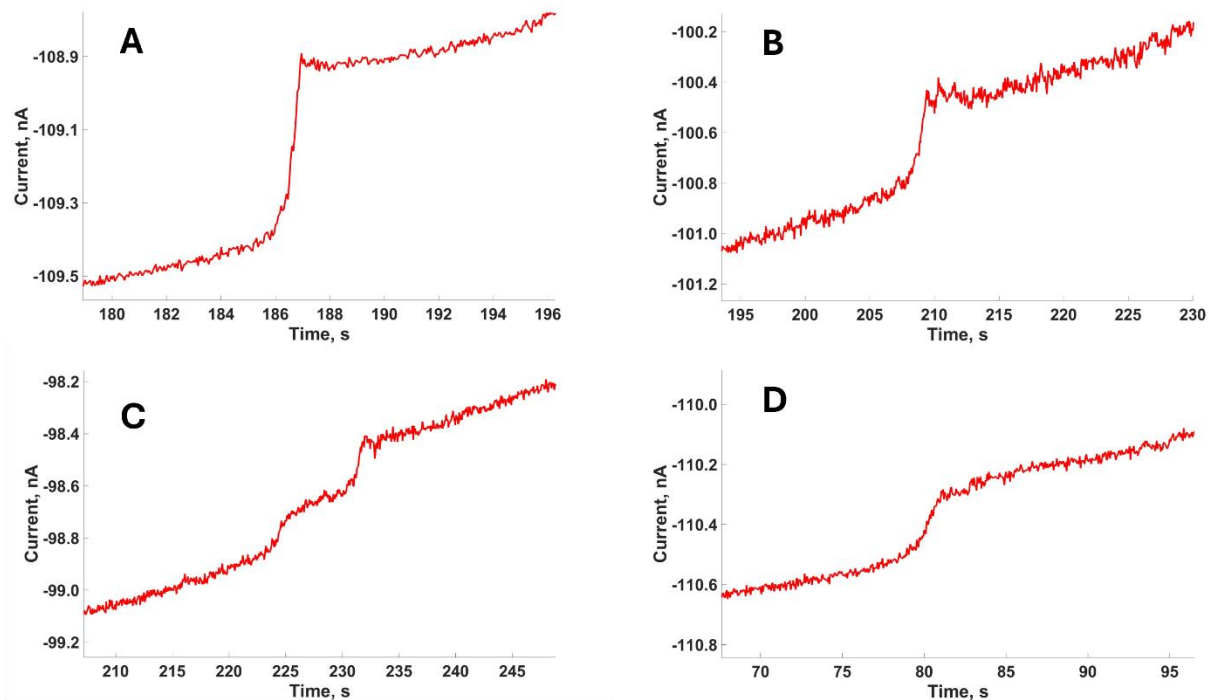


**Figure 28:** Four steps observed in  $i$ - $t$  curves recorded of *B. subtilis* 2 hours after ( $t = 2 \text{ hr}$ ) exposure to  $1 \mu\text{M}$  valinomycin. Here, mostly step-like signals are observed in A-D, though the first signal in C is significantly rounder in shape. In B, C, and D, an increase in signal variation is observed immediately following the step, which may be attributed to movement of the adsorbed cell

## 5.4. Conclusions

In conclusion, we have found that bacteria exposed to the antibiotic valinomycin exhibit changed behavior in chronoamperometric experiments, though additional work is required to fully quantify this change. The possible deviation in zeta potential of exposed bacteria may be the root cause of this changed behavior, but more experiments exploring the effect of valinomycin on zeta potential are required. Regardless, the step and signals observed in valinomycin-treated *B. subtilis* experiments are different than those observed in untreated *B. subtilis* experiments. The step-like signals observed in *B. subtilis* samples prior to exposure to valinomycin are transformed into hump-like signals post-exposure. Additionally, increased noise is observed after some bacteria-electrode collisions, regardless of their shape. The additional noise may be due to

movement of the bacteria at the surface of the electrode after the collision event, although this cannot be confirmed without visually monitoring the electrode throughout the electrochemical experiment. Future work should focus on quantifying these transient interactions via correlated microscopy to determine if the bacteria are leaving the electrode surface, shifting to block less flux, or otherwise moving after the collision event to produce the increased noise. Further, exposing the *B. subtilis* to increasing concentrations of valinomycin, from the MIC to 4X MIC, will help determine if the higher concentration results in a greater number of non-step-like signals. Overall, these first steps show that blocking electrochemistry can be used to monitor the efficacy of antibiotics on bacterial samples.

## Conclusions and Future Work

In this work, single-entity electrochemistry is expanded from the detection of bacterial cells at the surface of a disk ultramicroelectrode to the tentative identification of bacterial cells. The adsorption events of rod-shaped bacteria are thoroughly characterized, and equations are adapted from those for spherical particles. Interestingly, *A. erythreum* and *B. subtilis* are shown to adsorb at a frequency lower than predicted by migration alone, but higher than by diffusion alone, implying mixed mass transport of the bacterial cells to the electrode surface. A first-derivative Savitzky - Golay filter was used in Chapter 4 to transform the step-like signals to spikes, providing a flat background to determine the start and end points of each step more easily. Each step's current magnitude was calculated by integrating the area under each peak over the duration from peak start to peak end, which was in good agreement with results obtained from a manual analysis of the *i-t* curve. This data was used to create bidimensional population density plots, wherein each step's current magnitude and temporal aspect acted as a proxy for the bacteria's size. Finally, *B. subtilis* were exposed to valinomycin to determine if the efficacy of an antibiotic can be monitored by blocking electrochemistry. The signals observed in the *i-t* curves collected over time showed

that the signal changed from step-like signals to steps with post-adsorption noise or humps, where an initial rise was followed by a return to the baseline current.

The field of blocking electrochemistry offers exciting new possibilities for measurements at the lowest level of detection – the single entity. This work focuses on expanding the applications of blocking electrochemistry to bacterial identification and antibiotic efficacy monitoring. Future work should focus on expanding this work to create population density plots with other bacteria. It would also be useful to employ an internal standard that can be used to show the population density of a monodisperse particle adsorbing to a UME with non-homogenous current density. Exposing *B. subtilis* to more antibiotics, particularly those with different mechanisms of action, would also provide interesting insights into how the manner of cell death affects the signals observed in *i-t* curves. Overall, blocking electrochemistry has potential applications in many fields where rapid and cost-effective bacterial detection and identification is of the utmost importance.

## Appendix A. MatLab Script for Savitzky-Golay Filtering

```
clear
clc

DELIMITED = ',';
HEADER = 16; %Adjust to last line of heading text

%%Import Data

[file,path] = uigetfile('*.txt');
filename = horzcat(path,file);
data_import = importdata(filename,DELIMITED,HEADER);
data(:, :) = data_import.data;

%% Data is being pulled from the numbered columns -- adjust as appropriate

time(:, :) = data(:,1); % Time, s
I(:, :) = data(:,2) * 10^9; % Current, nA
dt = 0.05; % adjust for sampling rate

%% Establish window size

ncount = 'Enter the window size (5, 7, 9,....25) and press "Enter" ';
ncount = input(ncount);

%% Establish Savitzky-Golay reference table (SG coefficients and
normalization factors)

SGtable = (-(ncount-1)/2):(ncount-1)/2; % SG coefficients for quadratic
first-derivative filter

normquad = [10 28 60 110 182 280 408 570 770 1012 1300]; %Normalization
coefficients for quadratic first-derivative filter (only for window sizes 5-
25)

normco = normquad(:,1+((ncount-5)/2)); %Pulls normalization coefficient
for input window size (ncount)

%% SG Analysis

datawin = ones(size(time,1)-(ncount+1),ncount); %Create table of indices
for moving window to reference

for k = 1:(size(time,1)-(ncount+1))

    datawin(k, :) = k:k+(ncount-1);

    SGdata (k, :) = (1/(dt*normco))*(SGtable*I(datawin(k, :))); %Savitzky-Golay
first-derivative filtering
```

```

end

    SGtime = time(((ncount-1)/2+1):(end-(((ncount-1)/2)+2)),:); %Cut excess
time from beginning and end of time data to match SGdata length

%% plot i-t data

    Fig1Title = erase(file, '.txt')
    figure(1);
    plot(time,I, 'LineWidth',0.1, 'DisplayName', [Fig1Title], 'Color', 'r');
    legend('Location', 'northeast')
    xlabel('time (s)')
    ylabel('I/t (nA/s)')
    set(gca, 'TickLength', [0 0]);

    ax1 = gca;

    hold on

%% plot SG data

    figure(2);
    plot(SGtime, SGdata, 'LineWidth',0.1, 'DisplayName', ['MatLab '
num2str(ncount) ' pt SG Filter'], 'Color', 'r');
    legend('Location', 'northeast')
    xlabel('time (s)')
    ylabel('I/t (nA/s)')
    set(gca, 'TickLength', [0 0]);

    ax1 = gca;

    hold on

%% ID peaks based on average y-value and noise

    SGavg = mean(SGdata(3/dt:end,:)); %Find average from t = 3s to end of
expt. Remove 3 s to remove segment of exponential current decay

    SGNoise = std(SGdata(3/dt:end,:)); %Find noise from t = 3s to end of
expt. Remove 3 s to remove segment of exponential current decay

    [pks,locs] =
findpeaks(SGdata, 'MinPeakHeight', (SGavg+SGNoise), 'MinPeakDistance', (0.75/dt))
; %Identify peaks

%% Remove peaks with area under curve less than 0.01 nA

for k = 1:size(locs,1)

```

```

PkSizeDown = locs(k) - (0.1/dt);
PkSizeUp = locs(k) + (0.1/dt);

if PkSizeDown <= 0
    AUC(k) =
trapz(SGtime(1:(locs(k)+(0.1/dt))),SGdata(1:(locs(k)+(0.1/dt))));

elseif PkSizeUp >= size(SGtime)
    AUC(k) = trapz(SGtime((locs(k)-(0.1/dt)):end),SGdata((locs(k)-
(0.1/dt)):end));

else
    AUC(k) = trapz(SGtime((locs(k)-
(0.1/dt):(locs(k)+(0.1/dt))),SGdata((locs(k)-(0.1/dt):(locs(k)+(0.1/dt))));

end

end

notpeaks = AUC < 0.01;

locs(notpeaks) = [];

clear notpeaks

clear AUC

%% Remove non-peaks in exponential decay curve

for k = 1:size((nonzeros(locs<20/dt)),1) % Limits k to peak locations in
first 20 seconds of i-t curve

    PkSizeDown = locs(k) - (5/dt);

    if PkSizeDown <= 0

        PkChk(k) = 1; % If peak location is in first 5 seconds of i-t curve,
PkChk = 1

    else

        PkChk(k) = SGdata(locs(k))<SGdata(locs(k)-(4/dt)); %If peak current
is less than the current 4 seconds earlier, PkChk = 1

    end

end

exist PkChk;

PK = ans;

```

```

if PK == 1
    notpeaks = PkChk>0;
    locs(notpeaks) = []; %any location that equals 1 is not a peak, and thus
deleted
end

%% Plot remaining peaks and noise

    figure(2);
    FirstLocs = plot(SGtime(locs),SGdata(locs),'v','MarkerFaceColor',[0
0.4470 0.7410],'MarkerEdgeColor',[0 0.4470 0.7410]);

    ax2 = axes('Position',[.65 .65 .23 .23]); %Add inset to graph to plot
step corresponding to peak

%% Manually add extra peaks

    ExtraPks = input('Are there extra peaks that need to be added? [Y/N]
','s');

if ExtraPks == 'Y'

    NumEPs = input('How many extra peaks would you like to add? ');
    disp('Scroll to zoom. Click to exit zoom, then select the peak you would
like to add.')

    for k = 1:NumEPs

        zoom on
        w = waitforbuttonpress; %MatLab will allow you to zoom by hovering
over the graph and scrolling
        [x,y] = ginput(1);
        NewPeak = dsearchn(SGtime, x);

plot(SGtime(NewPeak),SGdata(NewPeak),'v','MarkerFaceColor','#7E2F8E','MarkerE
dgeColor','#7E2F8E');
        locs = sort(cat(1,locs,NewPeak));
        zoom out

    end

end

%% Select Peak Start and End Points

    disp('Scroll to zoom in and out of the peak. Click to exit zoom, then
click on the start and end points of the peak.')
    disp('If the yellow indicator is highlighting an incorrectly identified
peak, please select an area that encompasses 9 seconds or more.')

for k = 1:size(locs,1)

```

```

    if (locs(k) - 5/dt) <= 0
        upperlim = SGtime(locs(k) + 5/dt);
        set(ax1, 'XLim', [SGtime(1,1) upperlim]) %Sets the x-axis to zoom in on
a peak that starts within 5 seconds of the beginning of the i-t curve
        temp = plot(ax2, SGtime(1:locs(k)+2.5/dt, :), I(1:locs(k)+2.5/dt, :));
%Plots the corresponding step in the inset

        elseif size(SGtime,1) <= (locs(k)) + 5/dt
            lowerlim = SGtime(locs(k) - 5/dt);
            set(ax1, 'XLim', [lowerlim SGtime(end, :)]); %Sets the x-axis to zoom in
on a peak that ends within 5 seconds of the end of the i-t curve
            temp = plot(ax2, SGtime(locs(k)-2.5/dt:end, :), I(locs(k)-
2.5/dt:end, :)); %Plots the corresponding step in the inset

        else
            lowerlim = SGtime(locs(k) - 5/dt);
            upperlim = SGtime(locs(k) + 5/dt);
            set(ax1, 'XLim', [lowerlim upperlim]); %Sets the x-axis to zoom in on
peak k to within +/- 5 seconds
            temp = plot(ax2, SGtime(locs(k)-2.5/dt:locs(k)+2.5/dt, :), I(locs(k)-
2.5/dt:locs(k)+2.5/dt, :)); %Plots the corresponding step in the inset

        end

        pmark =
plot(ax1, SGtime(locs(k)), SGdata(locs(k)), 'v', 'MarkerFaceColor', 'y', 'MarkerEdg
eColor', 'y'); %Highlights the mark on the graph yellow

        zoom xon
        w = waitforbuttonpress;
        [x,y] = ginput(2);
        ind1 = dsearchn(SGtime, x(1)); %Find index of first data point
        ind2 = dsearchn(SGtime, x(2)); %Find index of second data point
        deltat(k) = x(2)-x(1); %Calculate delta t for peak k
        AUC(k) = trapz(SGtime(ind1:ind2), SGdata(ind1:ind2)); %Area under the
curve for peak k

        delete(pmark)
        delete(temp)
        cla(ax2, 'reset');

        PCheck = ismember(SGtime(locs(k)), SGtime(ind1:ind2, :));

        if PCheck == 0
            [M,N] = max(SGdata(ind1:ind2, :));
            TempSG = SGtime(ind1:ind2, :);
            M = TempSG(N);
            NewPeak = dsearchn(SGtime, M);

plot(SGtime(NewPeak), SGdata(NewPeak), 'v', 'MarkerFaceColor', '#7E2F8E', 'MarkerE
dgeColor', '#7E2F8E');
        locs = cat(1, locs, NewPeak);

```

```

end

xlim auto
ylim auto

end

hold off
zoom off

locs = sort(locs);

notpeaks = deltat > 9.000;
    deltat(notpeaks) = [];
    AUC(notpeaks) = [];

SGresults = table(AUC',deltat', 'VariableNames', ["delta_i", "delta_t"])

%% Reset

disp('When you are ready to continue, press any key')
pause;

close all %Closes all figures

disp('Please update dt if the sampling interval will change for the next
file analyzed');

```

## References

- (1) Bard, A. J.; Faulkner, L. R.; Others. Fundamentals and Applications. *Electrochemical methods* **2001**, 2 (482), 580–632.
- (2) Kissinger, P.; Heineman, W. R. *Laboratory Techniques in Electroanalytical Chemistry, Second Edition, Revised and Expanded*; CRC Press, 1996.
- (3) Srinivasan, S. ELECTRODE/ELECTROLYTE INTERFACES: STRUCTURE AND KINETICS OF CHARGE TRANSFER. In *Fuel Cells: From Fundamentals to Applications*; Srinivasan, S., Ed.; Springer US: Boston, MA, 2006; pp 27–92.
- (4) Zoski, C. G. *Handbook of Electrochemistry*; Elsevier, 2006.
- (5) Park, S.-J.; Seo, M.-K. Chapter 1 - Intermolecular Force. In *Interface Science and Technology*; Park, S.-J., Seo, M.-K., Eds.; Elsevier, 2011; Vol. 18, pp 1–57.
- (6) *Zeta Potential - An Introduction in 30 Minutes*; Malvern Instruments Worldwide, 2015. <https://www.research.colostate.edu/wp-content/uploads/2018/11/ZetaPotential-Introduction-in-30min-Malvern.pdf>.
- (7) Lu, S.-M.; Chen, J.-F.; Wang, H.-F.; Hu, P.; Long, Y.-T. Mass Transport and Electron Transfer at the Electrochemical-Confined Interface. *J. Phys. Chem. Lett.* **2023**, 14 (5), 1113–1123.
- (8) Heinze, J. Ultramicroelectrodes in Electrochemistry. *Angew. Chem. Int. Ed Engl.* **1993**, 32 (9), 1268–1288.
- (9) Cottrell, F. G. *Der Reststrom bei galvanischer Polarisation betrachtet als ein Diffusionsproblem*; W. Engelmann, 1903.
- (10) Mark Wightman, R. Microvoltammetric Electrodes. *Anal. Chem.* **1981**, 53 (9), 1125A-34A.
- (11) Montenegro, I.; Arlete Queirós, M.; Daschbach, J. L. *Microelectrodes: Theory and Applications*; Springer Science & Business Media, 2012.
- (12) Denuault, G.; Mirkin, M. V.; Bard, A. J. Direct Determination of Diffusion Coefficients by Chronoamperometry at Microdisk Electrodes. *J. Electroanal. Chem. Interfacial Electrochem.* **1991**, 308 (1), 27–38.

- (13) Elgrishi, N.; Rountree, K. J.; McCarthy, B. D.; Rountree, E. S.; Eisenhart, T. T.; Dempsey, J. L. A Practical Beginner's Guide to Cyclic Voltammetry. *J. Chem. Educ.* **2018**, *95* (2), 197–206.
- (14) Deng, Z.; Renault, C. Detection of Individual Insulating Entities by Electrochemical Blocking. *Current Opinion in Electrochemistry* **2021**, *25*, 100619.
- (15) Miller, E. S.; Woese, C. R.; Brenner, S. Description of the Erythromycin-Producing Bacterium *Arthrobacter* Sp. Strain NRRL B-3381 as *Aeromicrobium Erythreum* Gen. Nov., Sp. Nov. *Int. J. Syst. Bacteriol.* **1991**, *41* (3), 363–368.
- (16) Errington, J.; Aart, L. T. van der. Microbe Profile: *Bacillus Subtilis*: Model Organism for Cellular Development, and Industrial Workhorse. *Microbiology* **2020**, *166* (5), 425–427.
- (17) Lane, N. The Unseen World: Reflections on Leeuwenhoek (1677) 'Concerning Little Animals.' *Philos. Trans. R. Soc. Lond. B Biol. Sci.* **2015**, *370* (1666), 20140344.
- (18) Karamanou, M.; Panayiotakopoulos, G.; Tsoucalas, G.; Kousoulis, A. A.; Androutsos, G. From Miasmas to Germs: A Historical Approach to Theories of Infectious Disease Transmission. *Infez. Med.* **2012**, *20* (1), 58–62.
- (19) Bonnet, M.; Lagier, J. C.; Raoult, D.; Khelaifia, S. Bacterial Culture through Selective and Non-Selective Conditions: The Evolution of Culture Media in Clinical Microbiology. *New Microbes New Infect* **2020**, *34*, 100622.
- (20) Opal, S. M. A Brief History of Microbiology and Immunology. In *Vaccines: A Biography*; Artenstein, A. W., Ed.; Springer New York: New York, NY, 2010; pp 31–56.
- (21) Tsalik, E. L.; Bonomo, R. A.; Fowler, V. G., Jr. New Molecular Diagnostic Approaches to Bacterial Infections and Antibacterial Resistance. *Annu. Rev. Med.* **2018**, *69*, 379–394.
- (22) Gerace, E.; Mancuso, G.; Midiri, A.; Poidomani, S.; Zummo, S.; Biondo, C. Recent Advances in the Use of Molecular Methods for the Diagnosis of Bacterial Infections. *Pathogens* **2022**, *11* (6). <https://doi.org/10.3390/pathogens11060663>.
- (23) Quinn, B. M.; Van 't Hof, P. G.; Lemay, S. G. Time-Resolved Electrochemical Detection of Discrete Adsorption Events. *J. Am. Chem. Soc.* **2004**, *126* (27), 8360–8361.

- (24) Dick, J. E.; Renault, C.; Bard, A. J. Observation of Single-Protein and DNA Macromolecule Collisions on Ultramicroelectrodes. *J. Am. Chem. Soc.* **2015**, *137* (26), 8376–8379.
- (25) Dick, J. E.; Hilterbrand, A. T.; Strawsine, L. M.; Upton, J. W.; Bard, A. J. Enzymatically Enhanced Collisions on Ultramicroelectrodes for Specific and Rapid Detection of Individual Viruses. *Proc. Natl. Acad. Sci. U. S. A.* **2016**, *113* (23), 6403–6408.
- (26) Chung, J.; Hertler, P.; Plaxco, K. W.; Sepunaru, L. Catalytic Interruption Mitigates Edge Effects in the Characterization of Heterogeneous, Insulating Nanoparticles. *J. Am. Chem. Soc.* **2021**, *143* (45), 18888–18898.
- (27) Elliott, J.; Simoska, O.; Karasik, S.; Shear, J. B.; Stevenson, K. J. Transparent Carbon Ultramicroelectrode Arrays for the Electrochemical Detection of a Bacterial Warfare Toxin, Pyocyanin. *Anal. Chem.* **2017**, *89* (12), 6285–6289.
- (28) Chen, Y.; Liu, Y.; Wang, D.; Gao, G.; Zhi, J. Three-Mediator Enhanced Collisions on an Ultramicroelectrode for Selective Identification of Single *Saccharomyces Cerevisiae*. *Anal. Chem.* **2022**, *94* (37), 12630–12637.
- (29) Kim, J. W.; Aruchamy, G.; Kim, B.-K. Recent Advances in Single-Entity Electrochemistry for Metal Nanoparticle, Nanodroplet, and Bio-Entity Analysis. *Trends Analyt. Chem.* **2023**, *169*, 117358.
- (30) Kim, B.-K.; Boika, A.; Kim, J.; Dick, J. E.; Bard, A. J. Characterizing Emulsions by Observation of Single Droplet Collisions--Attoliter Electrochemical Reactors. *J. Am. Chem. Soc.* **2014**, *136* (13), 4849–4852.
- (31) Gao, G.; Wang, D.; Brocenschi, R.; Zhi, J.; Mirkin, M. V. Toward the Detection and Identification of Single Bacteria by Electrochemical Collision Technique. *Anal. Chem.* **2018**, *90* (20), 12123–12130.
- (32) Park, H.; Park, J. H. In Situ Monitoring of Collision and Recollision Events of Single Attoliter Droplets via Single-Entity Electrochemistry. *J. Phys. Chem. Lett.* **2020**, *11* (23), 10250–10255.

- (33) Ahmed, J. U.; Lutkenhaus, J. A.; Alam, M. S.; Marshall, I.; Paul, D. K.; Alvarez, J. C. Dynamics of Collisions and Adsorption in the Stochastic Electrochemistry of Emulsion Microdroplets. *Anal. Chem.* **2021**, *93* (22), 7993–8001.
- (34) Lemay, S. G.; Renault, C.; Dick, J. E. Particle Mass Transport in Impact Electrochemistry. *Current Opinion in Electrochemistry* **2023**, *39*, 101265.
- (35) Boika, A.; Thorgaard, S. N.; Bard, A. J. Monitoring the Electrophoretic Migration and Adsorption of Single Insulating Nanoparticles at Ultramicroelectrodes. *J. Phys. Chem. B* **2013**, *117* (16), 4371–4380.
- (36) Lee, J. Y.; Kim, B.-K.; Kang, M.; Park, J. H. Label-Free Detection of Single Living Bacteria via Electrochemical Collision Event. *Sci. Rep.* **2016**, *6*, 30022.
- (37) Ronspees, A. T.; Thorgaard, S. N. Blocking Electrochemical Collisions of Single *E. Coli* and *B. Subtilis* Bacteria at Ultramicroelectrodes Elucidated Using Simultaneous Fluorescence Microscopy. *Electrochim. Acta* **2018**, *278*, 412–420.
- (38) Stetefeld, J.; McKenna, S. A.; Patel, T. R. Dynamic Light Scattering: A Practical Guide and Applications in Biomedical Sciences. *Biophys. Rev.* **2016**, *8* (4), 409–427.
- (39) Kwon, S. J.; Zhou, H.; Fan, F.-R. F.; Vorobyev, V.; Zhang, B.; Bard, A. J. Stochastic Electrochemistry with Electrocatalytic Nanoparticles at Inert Ultramicroelectrodes—Theory and Experiments. *Phys. Chem. Chem. Phys.* **2011**, *13* (12), 5394–5402.
- (40) Lebègue, E.; Costa, N. L.; Louro, R. O.; Barrière, F. Communication—Electrochemical Single Nano-Impacts of Electroactive *Shewanella Oneidensis* Bacteria onto Carbon Ultramicroelectrode. *J. Electrochem. Soc.* **2020**, *167* (10), 105501.
- (41) Ho, T. L. T.; Hoang, N. T. T.; Lee, J.; Park, J. H.; Kim, B.-K. Determining Mean Corpuscular Volume and Red Blood Cell Count Using Electrochemical Collision Events. *Biosens. Bioelectron.* **2018**, *110*, 155–159.
- (42) Park, J. H.; Boika, A.; Park, H. S.; Lee, H. C.; Bard, A. J. Single Collision Events of Conductive Nanoparticles Driven by Migration. *J. Phys. Chem. C* **2013**, *117* (13), 6651–6657.
- (43) Thorgaard, S. N.; Jenkins, S.; Tarach, A. R. Influence of Electroosmotic Flow on Stochastic Collisions at Ultramicroelectrodes. *Anal. Chem.* **2020**, *92* (18), 12663–12669.

- (44) Zhao, H.; Chang, J.; Boika, A.; Bard, A. J. Electrochemistry of High Concentration Copper Chloride Complexes. *Anal. Chem.* **2013**, *85* (16), 7696–7703.
- (45) Boika, A.; Bard, A. J. Time of First Arrival in Electrochemical Collision Experiments as a Measure of Ultralow Concentrations of Analytes in Solution. *Anal. Chem.* **2015**, *87* (8), 4341–4346.
- (46) Mancuso, G.; Midiri, A.; Gerace, E.; Biondo, C. Bacterial Antibiotic Resistance: The Most Critical Pathogens. *Pathogens* **2021**, *10* (10). <https://doi.org/10.3390/pathogens10101310>.
- (47) Ahmed, J. U.; Lutkenhaus, J. A.; Tubbs, A.; Nag, A.; Christopher, J.; Alvarez, J. C. Estimating Average Velocities of Particle Arrival Using the Time Duration of the Current Signal in Stochastic Blocking Electrochemistry. *Anal. Chem.* **2022**, *94* (48), 16560–16569.
- (48) Myers, J. A.; Curtis, B. S.; Curtis, W. R. Improving Accuracy of Cell and Chromophore Concentration Measurements Using Optical Density. *BMC Biophys.* **2013**, *6* (1), 4.
- (49) Peterson, B. W.; Sharma, P. K.; van der Mei, H. C.; Busscher, H. J. Bacterial Cell Surface Damage Due to Centrifugal Compaction. *Applied and Environmental Microbiology*. 2012, pp 120–125. <https://doi.org/10.1128/aem.06780-11>.
- (50) Mukherjee, S.; Kearns, D. B. The Structure and Regulation of Flagella in *Bacillus Subtilis*. *Annu. Rev. Genet.* **2014**, *48*, 319–340.
- (51) Kinsinger, R. F.; Shirk, M. C.; Fall, R. Rapid Surface Motility in *Bacillus Subtilis* Is Dependent on Extracellular Surfactin and Potassium Ion. *J. Bacteriol.* **2003**, *185* (18), 5627–5631.
- (52) Tirado, M. M.; de la Torre, J. G. Rotational Dynamics of Rigid, Symmetric Top Macromolecules. Application to Circular Cylinders. *J. Chem. Phys.* **1980**, *73* (4), 1986–1993.
- (53) Tirado, M. M.; de la Torre, J. G. Translational Friction Coefficients of Rigid, Symmetric Top Macromolecules. Application to Circular Cylinders. *J. Chem. Phys.* **1979**, *71* (6), 2581–2587.
- (54) Deng, Z.; Elattar, R.; Maroun, F.; Renault, C. In Situ Measurement of the Size Distribution and Concentration of Insulating Particles by Electrochemical Collision on Hemispherical Ultramicroelectrodes. *Anal. Chem.* **2018**, *90* (21), 12923–12929.

- (55) Pendergast, A. D.; Renault, C.; Dick, J. E. Correlated Optical–Electrochemical Measurements Reveal Bidirectional Current Steps for Graphene Nanoplatelet Collisions at Ultramicroelectrodes. *Anal. Chem.* **2021**, *93* (5), 2898–2906.
- (56) Fosdick, S. E.; Anderson, M. J.; Nettleton, E. G.; Crooks, R. M. Correlated Electrochemical and Optical Tracking of Discrete Collision Events. *J. Am. Chem. Soc.* **2013**, *135* (16), 5994–5997.
- (57) Bonezzi, J.; Boika, A. Deciphering the Magnitude of Current Steps in Electrochemical Blocking Collision Experiments and Its Implications. *Electrochim. Acta* **2017**, *236*, 252–259.
- (58) Savitzky, A.; Golay, M. J. E. Smoothing and Differentiation of Data by Simplified Least Squares Procedures. *Anal. Chem.* **1964**, *36* (8), 1627–1639.
- (59) Bevington, P.; Keith Robinson, D. *Data Reduction and Error Analysis for the Physical Sciences*; McGraw-Hill Education, 2003.
- (60) Kowalska-Krochmal, B.; Dudek-Wicher, R. The Minimum Inhibitory Concentration of Antibiotics: Methods, Interpretation, Clinical Relevance. *Pathogens* **2021**, *10* (2). <https://doi.org/10.3390/pathogens10020165>.
- (61) Furlong, I. J.; Lopez Mediavilla, C.; Ascaso, R.; Lopez Rivas, A.; Collins, M. K. Induction of Apoptosis by Valinomycin: Mitochondrial Permeability Transition Causes Intracellular Acidification. *Cell Death Differ.* **1998**, *5* (3), 214–221.
- (62) Arjes, H. A.; Vo, L.; Dunn, C. M.; Willis, L.; DeRosa, C. A.; Fraser, C. L.; Kearns, D. B.; Huang, K. C. Biosurfactant-Mediated Membrane Depolarization Maintains Viability during Oxygen Depletion in *Bacillus Subtilis*. *Curr. Biol.* **2020**, *30* (6), 1011-1022.e6.
- (63) De Jong, M. H.; van der Drift, C.; Vogels, G. D. Proton-Motive Force and the Motile Behavior of *Bacillus Subtilis*. *Arch. Microbiol.* **1976**, *111* (1–2), 7–11.
- (64) Tempelaars, M. H.; Rodrigues, S.; Abee, T. Comparative Analysis of Antimicrobial Activities of Valinomycin and Cereulide, the *Bacillus Cereus* Emetic Toxin. *Appl. Environ. Microbiol.* **2011**, *77* (8), 2755–2762.

## Vita

Ashley Tubbs was born in Elkhart, Indiana in May 1995. She moved to Evansville, Indiana at 5 years old, where she lived for nearly two decades. She earned her B.S. in Chemistry and A.S. in Business, with concentrations in Marketing and Management from the University of Southern Indiana in 2019. During her undergraduate studies, she conducted research under the supervision of Dr. Jeffrey Seyler and Dr. Evan Milliam. In August of 2019, she entered graduate school at Virginia Commonwealth University to pursue her Ph.D. in Analytical Chemistry in the Alvarez Lab.

While at Virginia Commonwealth University, Ashley was heavily involved in the American Chemical Society of Virginia Local Section, becoming Chair of the ACS Virginia Younger Chemists Committee and Chair-elect of the ACS Virginia Local Section by 2024. She was also selected to serve as an associate member of the National Younger Chemists Committee in 2023, a position she continues to hold. In 2022, Ashley was recognized as the ACS Virginia Outreach Volunteer of the Year and received the Younger Leader Award, which allowed her to attend the ACS Leadership Institute in Atlanta, Georgia. In addition to her volunteer work, Ashley was also selected to receive the VCU Graduate School Dissertation Fellowship and the College of Humanities and Sciences Student Award for Graduate Student Teaching.